FLOW-BASED CONFORMAL PREDICTION FOR MULTI-DIMENSIONAL TIME SERIES

Anonymous authors
Paper under double-blind review

ABSTRACT

Time series prediction underpins a broad range of downstream tasks across many scientific domains. Recent advances and increasing adoption of black-box machine learning models for time series prediction highlight the critical need for reliable uncertainty quantification. While conformal prediction has gained attention as a reliable uncertainty quantification method, conformal prediction for time series faces two key challenges: (1) adaptively leveraging correlations in features and non-conformity scores to overcome the exchangeability assumption, and (2) constructing prediction sets for multi-dimensional outcomes. To address these challenges jointly, we propose a novel conformal prediction method for time series using flow with classifier-free guidance. We provide coverage guarantees by establishing exact non-asymptotic marginal coverage and a finite-sample bound on conditional coverage for the proposed method. Evaluations on real-world time series datasets demonstrate that our method constructs significantly smaller prediction sets than existing conformal prediction methods while maintaining target coverage.

1 INTRODUCTION

Uncertainty quantification has become essential in scientific fields where black-box machine learning models are widely deployed (Angelopoulos & Bates, 2021). Conformal prediction (CP) has emerged as a reliable, distribution-free framework for uncertainty quantification that constructs prediction sets with coverage guarantees, ensuring they contain the true outcome with a specified confidence level (Shafer & Vovk, 2008; Vovk et al., 2005). By constructing uncertainty sets using non-conformity scores that quantify how atypical predictions are, CP generates reliable prediction sets that satisfy a specified confidence level.

Time series prediction aims to forecast future outcomes based on past sequential observations of features (Box et al., 2015), and underpins a broad range of downstream tasks. Recent advances in machine learning have led to the development of various foundation models designed for time series prediction (Kim et al., 2025; Miller et al., 2024; Wen et al., 2023). The growing adoption of such models for time series prediction highlights the pressing need for reliable uncertainty quantification. Although CP has been actively studied for reliable uncertainty quantification, most existing CP methods rely on the assumption of data exchangeability (Barber et al., 2023). The exchangeability assumption is frequently violated in time series data, where observations exhibit complex temporal dependencies that induce correlations in the non-conformity scores, thereby making the direct application of CP to time series prediction particularly challenging. An additional challenge is that modern time series data often contain high-dimensional features and multi-

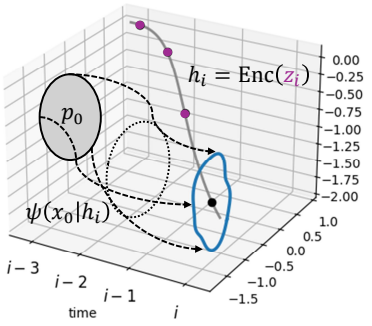

Figure 1: Our method adaptively constructs the prediction set at time i using a flow transformation ψ conditioned on guidance h_i, which encodes contextual information extracted from past features and residuals.

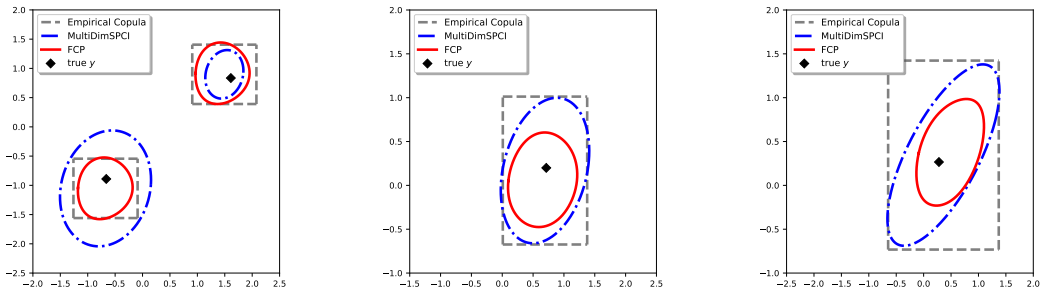

(a) Wind dataset (b) Traffic dataset (c) Solar dataset

Figure 2: Comparison of the prediction sets at a target coverage of 0.95, constructed by FCP (ours), MultiDimSPCI (Xu et al., 2024), and conformal prediction using empirical copula (Messoudi et al., 2021) on (a) wind, (b) traffic, and (c) solar datasets. Prediction sets are manually selected from the test set for visual clarity. Two prediction sets are shown for the wind dataset.

dimensional outcomes. While CP methods for univariate outcomes are well-established, extending these methods to generate prediction sets for multi-dimensional outcomes is not straightforward and requires careful consideration in constructing prediction sets.

There has been substantial effort to extend CP beyond the exchangeability assumption. One line of research focuses on addressing distribution shifts in the data (Barber et al., 2023; Tibshirani et al., 2019). More recently, several works have developed CP methods for time series. For example, Xu & Xie (2021a) proposed a method to construct sequential prediction intervals for time series based on a bootstrap ensemble estimator, which were later extended to incorporate conditional quantile estimation in order to exploit correlations in non-conformity scores (Xu & Xie, 2023b). Auer et al. (2024) used modern Hopfield networks to capture temporal dependencies by reweighting samples, and constructed prediction intervals based on these reweighting. Another line of work have proposed multi-step conformal prediction methods for time series, but they assume access to multiple i.i.d. sequences of time series (Stankeviciute et al., 2021; Sun & Yu, 2022), which may limit their applicability in general practical settings. Despite these efforts, existing methods remain limited to univariate outcomes or assume access to multiple i.i.d. time series.

Constructing prediction sets for multi-dimensional outcomes has been an active area of research. Early approaches used copulas (Messoudi et al., 2021) and ellipsoidal uncertainty sets (Henderson et al., 2024; Johnstone & Ndiaye, 2022; Messoudi et al., 2022), yielding hyper-rectangular and ellipsoidal prediction sets, respectively. Subsequent research has aimed to move beyond specific geometric shapes of prediction sets: Braun et al. (2025) formulated structured non-convex optimization to obtain minimum-volume sets; and Tumu et al. (2024) used convex templates for prediction sets. Recent works have focused on transporting multi-dimensional non-conformity scores to a reference distribution from which prediction sets can be constructed. For example, Klein et al. (2025) and Thurin et al. (2025) used Monge–Kantorovich ranks (Chernozhukov et al., 2017; Hallin et al., 2021) to map multi-dimensional non-conformity scores onto a reference distribution to construct prediction sets, by solving optimal transport problems. Fang et al. (2025) applied conditional normalizing flows to map multi-dimensional non-conformity scores to the source distribution and construct prediction sets using a calibration set with the source distribution.

Consequently, an effective CP method for time series prediction must address the two aforementioned challenges simultaneously: leveraging correlations in both features and non-conformity scores, and constructing prediction sets for multi-dimensional outcomes. To the best of our knowledge, Xu et al. (2024) is the only work that seeks to address both challenges jointly, constructing ellipsoidal prediction sets by defining non-conformity scores as the radii of ellipsoidal sets and predicting these non-conformity scores conditionally.

In this work, we propose a novel conformal prediction method designed for time series prediction with multi-dimensional outcomes. Our method is designed to effectively address the aforementioned two challenges by using flow with classifier-free guidance. Specifically, we use flow to model the distribution of prediction residuals and their transformations conditioned on historical context, which is encoded by using Transformer. We define the non-conformity score as the Euclidean distance between the transformed prediction residual and the mean of a Gaussian source distribution

of the flow, which allows us to construct prediction sets at a desired confidence level. We provide theoretical coverage guarantees by establishing an exact non-asymptotic marginal coverage and a finite-sample bound on conditional coverage for the proposed method. Empirical evaluations on three real-world multi-dimensional time series datasets demonstrate that the proposed method constructs significantly smaller prediction sets while maintaining target coverage, outperforming existing baselines.

2 Problem Setup

We consider a sequence of observations $\{(x_i, y_i) : i = 1, 2, \ldots\}$, where $x_i \in \mathbb{R}^{d_x}$ represents d_x-dimensional feature, and $y_i \in \mathbb{R}^{d_y}$ represents d_y-dimensional continuous outcome. We assume that we have a base predictor $\hat{f}$ that provides a point prediction $\hat{y}_i$ for y_i, given by $\hat{y}_i = \hat{f}(x_{(i-k):i})$, where k specifies the size of the past observation window. The base predictor $\hat{f}$ can be any black-box model and is not restricted to any specific constraints.

Suppose that the first T examples, $\{(x_i, y_i)\}_{i=1}^{T}$, are used for training. Our goal is to sequentially construct a prediction set $\hat{C}_i(z_i, \alpha)$ for the next step, beginning at time $i = T + 1$. Here, z_i denotes the features used to construct $\hat{C}_i$, and $\alpha \in [0, 1]$ denotes a pre-specified significance level. In the simplest setting, z_i consists only of x_i, but it may also include past features or non-conformity scores. We aim to construct prediction sets that satisfy *marginal coverage*:

$$\mathbb{P}\left(y_i \in \hat{C}_i(z_i, \alpha)\right) \geq 1 - \alpha, \quad \forall i, \tag{1}$$

and ideally *conditional coverage*:

$$\mathbb{P}\left(y_i \in \hat{C}_i(z_i, \alpha) \mid z_i\right) \geq 1 - \alpha, \quad \forall i. \tag{2}$$

Although trivially large prediction sets can always satisfy the target coverage, they do not provide useful information for uncertainty quantification. Therefore, the meaningful objective is to construct efficient prediction sets—the prediction sets that are as small as possible while satisfying the target coverage (Vovk et al., 2005).

Throughout this paper, we distinguish between the indices i and t to avoid confusion: the subscript i refers to the discrete time index of the sequence of observations, while the subscript t is reserved to refer to continuous time in ODEs. We use uppercase letters (e.g., X) to denote random variables and lowercase letters (e.g., x) to denote their realizations.

3 Method

3.1 Preliminary: Guided Flow

We use x as a generic variable in this section, distinct from the time series feature x_i introduced in the problem setup. A flow is a time-dependent mapping $\psi : [0, 1] \times \mathbb{R}^d \to \mathbb{R}^d$ that push-forward a random variable $X_0 \in \mathbb{R}^d$ from a source distribution p_0 to $X_t \in \mathbb{R}^d$ from a time-dependent probability density (i.e., probability path) p_t for time $t \in [0, 1]$ as follows:

$$([\psi_t]_* p_0)(x_t) = p_0(\psi_t^{-1}(x_t)) \left| \det \frac{\partial \psi_t^{-1}}{\partial x_t}(x_t) \right|, \tag{3}$$

where $*$ denotes the push-forward operator, $\det(\cdot)$ denotes the determinant, and $\psi_t(x) := \psi(t, x)$. Flow ψ is defined by a vector field $u : [0, 1] \times \mathbb{R}^d \to \mathbb{R}^d$ through the following ordinary differential equation (ODE):

$$\begin{aligned} \frac{d}{dt}\psi_t(x_0) &= u_t(\psi_t(x_0)), && \text{(flow ODE)} \\ \psi_0(x_0) &= x_0. && \text{(initial condition)} \end{aligned} \tag{4}$$

A guided flow $\psi_{t|h} : [0, 1] \times \mathbb{R}^d \times \mathbb{R}^{d_h} \to \mathbb{R}^d$ enables conditional generation by learning a mapping from a source distribution to a target conditional distribution, and is defined by a guided vector field

$u_{t|h} : [0,1] \times \mathbb{R}^d \times \mathbb{R}^{d_h} \to \mathbb{R}^d$ with the following ODE:

$$\begin{aligned} \frac{d}{dt}\psi_{t|h}(x_0 \mid h) &= u_{t|h}\left(\psi_{t|h}(x_0 \mid h) \mid h\right), \qquad \text{(guided flow ODE)} \\ \psi_{t=0|h}(x_0 \mid h) &= x_0, \qquad \text{(initial condition)} \end{aligned} \tag{5}$$

where $h \in \mathbb{R}^{d_h}$ denotes the guidance. By appropriately designing a conditional probability path per sample x_1 interpolating $p_{0|x_1}(x \mid x_1) = p_0$ and $p_{1|x_1}(x \mid x_1) = \delta_{x_1}$, where δ_{x_1} denoting the Dirac delta distribution centered at x_1, we can obtain the marginal guided probability path:

$$p_{t|h}(x \mid h) = \int p_{t|x_1}(x \mid x_1)\, q(x_1 \mid h)\, dx_1, \tag{6}$$

which interpolates the source distribution p_0 and the target conditional distribution $q(x_1 \mid h)$. Given the conditional vector field $u_{t|x_1}$ that generates each conditional path $p_{t|x_1}$, the marginal guided vector field is obtained as:

$$u_{t|h}(x \mid h) = \int u_{t|x_1}(x \mid x_1) \frac{p_{t|x_1}(x \mid x_1) q(x_1 \mid h)}{p_{t|h}(x \mid h)}\, dx_1. \tag{7}$$

One can verify the marginal guided vector field generates the marginal guided probability path using the *continuity equation* (see Proposition A.1). Therefore, in order to learn the target conditional distribution, we parameterize the guided vector field with neural networks and train it to approximate the marginal guided vector field as closely as possible. A simple and effective way to train the guided vector field is through flow matching, which minimizes the mean-squared error between the conditional guided vector field and the parameterized guided vector field (Lipman et al., 2022):

$$\mathcal{L}_{\text{CFM}} = \mathbb{E}_{t,(x_1,h)}\left[\left\| u^{\theta}_{t|h}(x \mid h) - u_{t|x_1}(x \mid x_1) \right\|^2\right], \tag{8}$$

where $t \sim \text{Unif}[0,1]$, $(x_1, h) \sim q_{\text{data}}$, and $u^{\theta}_{t|h}$ is the parameterized guided vector field with parameters θ.

We consider Gaussian conditional probability path defined as $p_{t|x_1}(x \mid x_1) = \mathcal{N}(x \mid \alpha_t x_1, \sigma_t^2 I_d)$, where $\mathcal{N}$ denotes the Gaussian kernel and $I_d \in \mathbb{R}^{d \times d}$ denotes the identity matrix. $\alpha_t, \sigma_t : [0,1] \to [0,1]$ are interpolating scheduler, which are smooth functions satisfying $\alpha_0, \sigma_1 = 0$, $\alpha_1, \sigma_0 = 1$, and $\frac{d}{dt}\alpha_t - \frac{d}{dt}\sigma_t > 0$ for $t \in (0,1)$. The guided vector field $u_{t|h}(x \mid h)$ can be reformulated as:

$$u_{t|h}(x \mid h) = u_t(x) + b_t \nabla_x \log p_{h|t}(h \mid x), \tag{9}$$

where $u_t(x)$ is unguided vector field, b_t is a scalar constant regarding α_t and σ_t (see Proposition A.2). Based on this reformulation, early approaches trained a separate classifier (Song et al., 2020) with a classifier scale $w > 1$ is beneficial in conditional generation in practice (Dhariwal & Nichol, 2021) :

$$\tilde{u}_{t|h}(x \mid h) = u_t(x) + w b_t \nabla_x \log p_{h|t}(h \mid x). \tag{10}$$

By using the identity $\nabla_x \log p_{t|h}(x \mid h) = \nabla_x \log p_t(x) + \nabla_x \log p_{h|t}(h \mid x)$, equation (10) can be equivalently rewritten as:

$$\tilde{u}_{t|h}(x \mid h) = (1-w) u_t(x) + w u_{t|h}(x \mid h). \tag{11}$$

Instead of modeling $u_t(x)$ and $u_t(x \mid h)$ separately, Ho & Salimans (2022) proposed using a single vector field to model both cases by assigning a null condition $h_\varnothing$ to represent the unguided vector field, which is known as classifier-free guidance (CFG):

$$\tilde{u}_{t|h}(x \mid h) = (1-w) u_{t|h}(x \mid h_\varnothing) + w u_{t|h}(x \mid h), \tag{12}$$

where $h_\varnothing$ denotes the guidance representing the unguided state of the vector field. The guided vector field can be trained using flow matching with the loss:

$$\mathcal{L}^{\text{CFG}}_{\text{CFM}} = \mathbb{E}_{t,\eta,(x_1,h)}\left[\left\| u^{\theta}_{t|h}(x \mid (1-\eta)h + \eta h_\varnothing) - u_{t|x_1}(x \mid x_1) \right\|^2\right], \tag{13}$$

where $\eta \sim \text{Bernoulli}(p_\varnothing)$ and $p_\varnothing$ denotes the probability of assigning $h_\varnothing$. The resulting guided vector field $\tilde{u}_{t|h}(x \mid h)$ in equation (12) enables conditional generation by solving the guided flow ODE and has been widely used in various tasks such as image generation (Esser et al., 2024) and video generation (Polyak et al., 2025).

Algorithm 1: Training Guided Flow using Flow Matching

Input: $p_\varnothing$, initialized $u^\theta_{t|h}$ and Enc^θ
while *not converged* **do**
  $\hat{\epsilon}_i \leftarrow y_i - \hat{y}_i$ ▷ obtain prediction residuals
  $h_i \leftarrow \text{Enc}^\theta(z_i)$ ▷ obtain contextual representation
  $h_i \leftarrow h_\varnothing$ with probability $p_\varnothing$ ▷ assign unguided state with probability $p_\varnothing$
  $x_0 \sim p_0(x)$
  $t \sim \text{Unif}(0, 1)$
  $x_t \leftarrow \alpha_t \hat{\epsilon} + \sigma_t x_0$
  $u_{t|\hat{\epsilon}} \leftarrow \frac{d}{dt}\alpha_t \hat{\epsilon}_i + \frac{d}{dt}\sigma_t x_0$
  Update with $\nabla_\theta \| u^\theta_{t|h}(x_t, h_i) - u_{t|\hat{\epsilon}} \|^2$ ▷ flow matching loss
Output: trained $u^\theta_{t|h}$ and Enc^θ

3.2 Conformal Prediction for Time Series using Guided Flow

We use guided flow to learn a mapping from the source distribution to the distribution of prediction residual $\hat{\epsilon} = y - \hat{y}$, conditioned on past features and residuals. The prediction set is then defined through this transformation using guided flow to achieve the target coverage. This construction effectively addresses the two aforementioned key challenges in conformal prediction for time series. First, the guided flow explicitly captures correlations among past features and residuals by using them as guidance. Second, since the transformation using the guided flow can be defined between random variables in arbitrary dimensions, it enables the generation of prediction sets for multi-dimensional outcomes in any $\mathbb{R}^{d_y}$. Figure 1 provides a visual illustration of the method. We describe the method in detail in this section.

Guided flow design. We use Gaussian probability path with interpolating scheduler $a_t = t$ and $\sigma_t = (1 - t)$. The source distribution is set to an isotropic Gaussian with zero mean and covariance scale $\gamma > 0$, i.e., $\mathcal{N}(0, \gamma I_{d_y})$. For each time index i, we construct z_i by concatenating the past w features and prediction residuals, and use an encoder to obtain a contextual representation $h_i = \text{Enc}(z_i)$. The classifier-free guided vector field as defined in equation (12) uses h_i as the guidance to model the conditional distribution of $\hat{\epsilon}_i$. In our method, we use Transformer as the encoder (Vaswani et al., 2017), though alternative sequence models such as recurrent neural networks (RNNs) are also applicable. The guided vector field is trained via flow matching as defined in equation (13), and the encoder is jointly trained with it. The overall training procedure is summarized in Algorithm 1.

Prediction set. The trained guided flow models the conditional distribution of the prediction residual by mapping samples from the source Gaussian distribution to residuals conditioned on the guidance h_i. Since this transformation is bijective, we can define prediction sets for the residuals directly through the transformation. Let $\hat{e}_i(y) := ||\psi^{-1}_{t=1|h}(\hat{\epsilon} \mid h_i)||$ be the Euclidean distance between the transformed residual and the origin, then the prediction set at significance level α can be defined as:

$$\hat{C}_i(z_i, \alpha) = \{y : \hat{e}_i(y) \leq r_{1-\alpha}\}, \tag{14}$$

where $r_{1-\alpha}$ is the radius of the ball $\mathcal{B}_{1-\alpha}$ that contains $1 - \alpha$ probability mass. Since we use $\mathcal{N}(0, \gamma I_{d_y})$ as the source distribution, the radius $r_{1-\alpha}$ is given by $r_{1-\alpha} = \sqrt{\gamma}\chi^{-1}_{d_y}(1-\alpha)$, where $\chi^{-1}_{d_y}$ denotes the inverse cumulative distribution function (CDF) of the chi distribution with d_y degrees of freedom. Intuitively, the prediction set is obtained by taking the ball that contains the same amount of probability mass as the target coverage and transforming it to the prediction set for the residual using the guided flow. Although this construction directly uses $\hat{e}(y)$ to construct the prediction set, $\hat{e}(y)$ is computed from the transformed residual and therefore serves as a proxy non-conformity score, consistent with treating residuals as non-conformity scores.

Since the prediction set is obtained through the transformation using the guided flow, it can take on flexible shapes without being constrained to follow any fixed geometric form, such as convex or ellipsoidal sets. We believe this enables the guided flow to generate smaller prediction sets that are better aligned with the data and the guidance. Although the prediction sets do not have any fixed geometric shape, some useful topological properties can still be inferred. In particular, Theorem A.4

ensures that the prediction sets are closed and connected. Figure 2 shows prediction sets in $\mathbb{R}^2$ generated by our proposed method alongside two other methods that produce hyper-rectangular prediction sets (Messoudi et al., 2021) and ellipsoidal prediction sets (Xu et al., 2024). The figure visually demonstrates the flexible shapes of the prediction sets constructed by our proposed method.

The size of the prediction set is computed as:

$$\int_{\mathcal{B}_\alpha} \left|\det\left(J_{\psi_{t=1|h}}(x \mid h)\right)\right| \, dx \approx \text{Size}(\mathcal{B}_\alpha)\frac{1}{N}\sum_{j=1}^{N}\left|\det(J_{\psi_{t=1|h}}(x_j \mid h))\right|, \tag{15}$$

where ψ_1 represents the flow transformation from $t = 0$ to $t = 1$, and $J_{\psi_1}(x \mid h)$ denotes the Jacobian of ψ_1 at $x \in \mathcal{B}_\alpha$ conditioned on h. The right-hand side provides a Monte Carlo approximation, where x_j are i.i.d. samples drawn from $\mathcal{B}_\alpha$ and N is the number of samples. However, directly computing $\det\left(J_{\psi_1}(x \mid h)\right)$ is computationally expensive, as it requires solving the guided flow ODE and evaluating the full Jacobian matrix. Instead, we can compute the log-determinant of the Jacobian by solving the following ODE:

$$\begin{aligned} \frac{d}{dt}\log\left|\det J_{\psi_{t|h}}(x \mid h)\right| &= \text{div}\left(u_{t|h}(\psi_{t|h}(x \mid h) \mid h)\right), && \text{(Jacobian ODE)} \\ \log\left|\det\left(J_{\psi_{t=0|h}}(x \mid h)\right)\right| &= 0, && \text{(initial condition)} \end{aligned} \tag{16}$$

where $\text{div}(\cdot)$ denotes the divergence operator. A detailed derivation is provided in Proposition A.3. The accuracy of the prediction set size estimate depends on the Monte Carlo approximation. Purely random sampling from $\mathcal{B}_\alpha$ may introduce bias due to uneven coverage of the sampling space, and a small sample size N can result in high variance. To reduce sampling bias, we use quasi-Monte Carlo sampling based on Sobol sequences (Sobol, 1967; Owen, 2023), which provides more uniform sampling from $\mathcal{B}_\alpha$. To control variance from finite sampling, we monitor the relative error in terms of sample size N. Additional implementation details are provided in the experiment section.

4 Theory

In this section, we present exact non-asymptotic marginal coverage and a finite-sample bound on conditional coverage. We assume that $y_i \in \mathbb{R}^{d_y}$ is generated from an unknown true function f with additive noise $\epsilon_i \in \mathbb{R}^{d_y}$ according to $y_i = f(x_{(i-k):i}) + \epsilon_i$. Proofs are presented in Appendix A.

4.1 Marginal Coverage

We first establish that prediction sets generated by our method achieve exact non-asymptotic marginal coverage. This result follows from a fundamental property of flow: probability mass preservation under push-forward operations. When any measurable set is transformed through the push-forward operation of a flow, its probability mass is preserved. Lemma 4.3 formalizes this property and suffices to prove the exact non-asymptotic marginal coverage stated in Proposition 4.4.

Assumption 4.1 (Flow existence and uniqueness)**.** The guided vector field $u_t(x \mid h)$ is continuously differentiable and Lipschitz continuous in x for all t and h. That is, there exists a constant $L_u > 0$ such that

$$\|u_t(x \mid h) - u_t(x' \mid h)\| \le L_u\|x - x'\|, \quad \forall t, h, x, x'. \tag{17}$$

Remark 4.2. Assumption 4.1 ensures the existence and uniqueness of solutions of the guided flow ODE. In practice, the guided vector field can be modeled using neural network architectures that satisfy this assumption, such as multi-layer perceptrons (MLP) with smooth activation functions.

Lemma 4.3 (Probability mass preserving property of flows)**.** *Let $X \sim p_X$ be a continuous random variable on $\mathbb{R}^d$, and let $\psi : \mathbb{R}^d \to \mathbb{R}^d$ be a C^1 diffeomorphism. Define $Y := \psi(X)$ with density p_Y given by the push-forward of p_X under ψ. Then, for any measurable set $\mathcal{A} \subset \mathbb{R}^d$, the transformed set $\mathcal{A}' := \psi(\mathcal{A})$ satisfies:*

$$\mathbb{P}(X \in \mathcal{A}) = \mathbb{P}(Y \in \mathcal{A}') \tag{18}$$

Proposition 4.4 (Marginal coverage)**.** *Let $\alpha \in (0, 1)$ be a pre-specified significance level. Under Assumption 4.1, suppose the guided flow provides a sufficiently accurate approximation of the target distribution from the source distribution. If the ball $\mathcal{B}_{1-\alpha}$ defining the prediction set in equation (14) has probability mass $1 - \alpha$, then the prediction set achieves exact marginal coverage of $1 - \alpha$.*

4.2 CONDITIONAL COVERAGE

We next establish a finite-sample bound on conditional coverage. We define the non-conformity score based on the prediction residual as $\hat{e}_i = ||\psi^{-1}(\hat{\epsilon}_i \mid h_i)||$, and the non-conformity score based on the true noise as $e_i = ||\psi^{-1}(\epsilon_i \mid h_i)||$. The guided flow ψ is trained on the training set until convergence and then fixed for computing e and $\hat{e}$. The empirical CDF of $\hat{e}$ and e are defined as:

$$\hat{F}_{T+1}(u) = \frac{1}{T}\sum_{i=1}^{T} \mathbb{1}\{\hat{e}_i \le u\}, \quad \tilde{F}_{T+1}(u) = \frac{1}{T}\sum_{i=1}^{T} \mathbb{1}\{e_i \le u\}. \tag{19}$$

We denote $F_e(u) = \mathbb{P}(e \le u)$ as the CDF of the true non-conformity scores. Since the source distribution of the guided flow in our method is set to be identical across time, the marginal distribution for e_i can be considered to be identical for all i. However, while the marginal distribution of e_i is identical for all i, they may exhibit dependence through h_i. Therefore, we consider two settings: (1) when $\{e_i\}_{i=1}^{T+1}$ are i.i.d., and (2) when $\{e_i\}_{i=1}^{T+1}$ are stationary and strongly mixing. We first establish a finite-sample bound on conditional coverage under the assumption of i.i.d. non-conformity scores.

Assumption 4.5 (i.i.d. non-conformity scores)**.** The true non-conformity scores $\{e_i\}_{i=1}^{T}$ are i.i.d.

Assumption 4.6 (Bi-Lipschitz flow)**.** We assume that the guided flow $\psi_t(x \mid h)$ is bi-Lipschitz continuous in x for all t and h. That is, there exist constants $L_\psi > 0$ and $L_{\psi^{-1}} > 0$, such that

$$\|\psi_t(x \mid h) - \psi_t(x' \mid h)\| \le L_\psi \|x - x'\|, \quad \forall t, h, x, x', \tag{20}$$

and

$$\|\psi_t^{-1}(x \mid h) - \psi_t^{-1}(x' \mid h)\| \le L_{\psi^{-1}} \|x - x'\|, \quad \forall t, h, x, x'. \tag{21}$$

Remark 4.7. Lemma A.8 shows that bi-Lipschitz guided vector field results in bi-Lipschitz guided flow. Therefore, the vector field $u_t(x \mid h)$ can be modeled using neural network architectures that satisfy this assumption. For example, one can use invertible Residual Networks (iResNet) (Behrmann et al., 2019; Chen et al., 2019) with smooth activation functions.

Assumption 4.8 (Lipschitz continuous of the CDF of the true non-conformity scores)**.** Assume that $F_e(u)$ is Lipschitz continuous with Lipschitz constant $L_{T+1} > 0$, and that F_e is strictly increasing in u.

Assumption 4.9 (Estimation quality)**.** Define $\Delta_i = \hat{\epsilon}_i - \epsilon_i$. There exists a sequence $\{\delta_T\}_{T\ge 1}$ such that

$$\frac{1}{T}\sum_{i=1}^{T} \|\Delta_i\|^2 \le \delta_T^2, \quad \|\Delta_{T+1}\| \le \delta_T. \tag{22}$$

As a result of Lemma A.10 and A.15, Theorem 4.10 establishes the finite-sample bound for conditional coverage under i.i.d. non-conformity scores.

Theorem 4.10 (Conditional coverage bound under i.i.d. non-conformity scores)**.** *Under Assumption 4.5, 4.6, 4.8, and 4.9, suppose the guided flow provides a sufficiently accurate approximation of the target distribution from the source distribution. With probability* $1-\delta$*, we have:*

$$\begin{aligned} &\left|\mathbb{P}(Y_{T+1} \in \widehat{C}^{\alpha}_{T+1} \mid Z_{T+1} = z_{T+1}) - (1-\alpha)\right| \\ &\le 12\sqrt{\frac{\log(16T)}{T}} + 4(L_{T+1} + \frac{1}{2})(2C + \delta_T). \end{aligned} \tag{23}$$

Assumption 4.11 (Strictly stationary and strongly mixing non-conformity scores)**.** Assume that the sequence $\{e_i\}_{i=1}^{T}$ is strictly stationary and strongly mixing, with mixing coefficients satisfying $0 < \sum_{k>0} \alpha(k) < M < \infty$.

Corollary 4.12 (Conditional coverage bound under stationary and strongly mixing non-conformity scores)**.** *4.6, 4.8, 4.9, and 4.11, suppose the guided flow provides a sufficiently accurate approximation of the target distribution from the source distribution. With probability* $1-\delta$*, we have:*

$$\begin{aligned} &\left|\mathbb{P}(Y_{T+1} \in \widehat{C}^{\alpha}_{T+1} \mid Z_{T+1} = z_{T+1}) - (1-\alpha)\right| \\ &\le 12\frac{(\frac{M}{2})^{1/3}(\log T)^{2/3}}{T^{1/3}} + 4(L_{T+1} + \frac{1}{2})(2C + \delta_T). \end{aligned} \tag{24}$$

The bounds in Theorem 4.10 and Corollary 4.12 depend on the sample size T and the estimation error δ_T. Both bounds converge to $1-\alpha$ as $T \to \infty$, provided that $\delta_T = \mathcal{O}(T^{-a})$ for some $a > 0$. Intuitively, with sufficiently large training data and an accurate base predictor $\hat{f}$, the conditional coverage is guaranteed. The condition on δ_T can be satisfied by a broad class of estimators. For example, sieve estimators based on general neural networks achieve $\delta_T = o_p(T^{-1/4})$ when f is sufficiently smooth (Chen & White, 1999). The Lasso estimator and Dantzig selector achieve $\delta_T = o_p(T^{-1/2})$ when f is a sparse high-dimensional linear model (Bickel et al., 2009).

5 EXPERIMENTS

For notational convenience, we refer to our method as FCP, which stands for Flow-based Conformal Prediction. We use MLP with Softplus activation to model the guided vector field and concatenate the guidance and time with the input for the MLP. `dopri5` (Dormand & Prince, 1980) at absolute and relative tolerances of 1e-5 is used to solve all ODEs. A grid search is conducted to select the optimal hyperparameters for FCP. To determine an appropriate sample size N, we compute the relative standard error (SE) of the Jacobian determinants of ψ, defined as $\text{SE}\left(\{\det J_\psi(x_j \mid h)\}_{j=1}^N\right) / \text{Avg}\left(\{\det J_\psi(x_j \mid h)\}_{j=1}^N\right)$, then choose the smallest N such that the average relative SE across all h falls below 0.01. The source code for FCP is available at `anonymous_url`.

Baselines. We evaluate FCP against several conformal prediction methods covering various existing approaches: MultiDimSPCI (Xu et al., 2024), OT-CP (Thurin et al., 2025), CONTRA (Fang et al., 2025), conformal prediction using local ellipsoids (Messoudi et al., 2022), CopulaCPTS (Sun & Yu, 2022), and conformal prediction using empirical and Gaussian copulas (Messoudi et al., 2021). We also include two widely used probabilistic time series forecasting methods as baselines: Temporal Fusion Transformer (TFT) (Lim et al., 2021) and DeepAR (Salinas et al., 2020). Although TFT and DeepAR are originally developed for time series with univariate outcomes, we adapt them to our multi-dimensional setting by constructing independent copulas using the predicted intervals for each output dimension. Additional details and setup of the baselines are provided in Appendix B.

Datasets and base predictor. We evaluated FCP and baselines on three real-world time series datasets: wind, traffic, and solar datasets. For the wind and traffic datasets, we randomly selected $d_y \in \{2, 4, 8\}$ locations to construct five sequences of d_y-dimensional time series. For the solar dataset, we use $d_y \in \{2, 4\}$ and similarly construct five sequences. Additional dataset details are provided in Appendix C. Base predictor $\hat{f}$ is required to provide a point prediction $\hat{y}$. We used two types of base predictors for each dataset: (1) leave-one-out (LOO) bootstrap ensemble of 15 multivariate linear regressors, and (2) recurrent neural network (RNN) with long short-term memory (LSTM) units (Hochreiter & Schmidhuber, 1997). Since the RNN base predictor requires part of the sequence for training, whereas the LOO bootstrap predictor can leverage the full sequence, the effective sequence length available for evaluation varies by predictor. Each base predictor was trained independently for every sequence. For the RNN base predictor, the first 50% of each sequence was allocated for training, and predictions were made for the remaining 50%, which served as the evaluation sequence. Within this evaluation sequence, the first 80% was used as a training set, and the final 20% was evenly divided into validation and test sets. Since FCP does not require a calibration set to construct prediction sets, the validation set was used for model selection during training. To ensure fair evaluation in terms of data utilization, we combined the training and validation sets into a single calibration set for methods that require a calibration set. The specific data utilization scheme for each baseline is detailed Appendix B.

Evaluation metrics. Efficient prediction sets are those that are as small as possible while satisfying the desired coverage. Therefore, we use two evaluation metrics: empirical coverage and the average prediction set size. The empirical coverage at a target confidence level α is defined as:

$$\frac{1}{|\mathcal{D}_{\text{test}}|} \sum_{\{z_i, y_i\} \in \mathcal{D}_{\text{test}}} \mathbb{1}\left(y_i \in \hat{C}_i(z_i, \alpha)\right), \tag{25}$$

Table 1: Average empirical coverage and prediction sets sizes obtained by FCP and all baselines on three real-world datasets, evaluated under different base predictors and varying outcome dimensions d_y. Reported values represent the average and standard deviation over five independent experiments. The target confidence level was set to 0.95. Results with average empirical coverage below the target confidence level are grayed out, and the smallest prediction set sizes, excluding the grayed-out results, are highlighted in bold.

Dataset	Base Predictor	Method	$d_y = 2$		$d_y = 4$		$d_y = 8$	
			Coverage	Size	Coverage	Size	Coverage	Size
Wind	LOO Bootstrap	FCP	$0.951_{\pm.018}$	$\mathbf{0.88}_{\pm.089}$	$0.953_{\pm.006}$	$\mathbf{3.43}_{\pm1.37}$	$0.956_{\pm.010}$	$\mathbf{19.4}_{\pm10.2}$
		MultiDimSPCI	$0.953_{\pm.016}$	$1.31_{\pm.524}$	$0.956_{\pm.018}$	$6.39_{\pm3.90}$	$0.951_{\pm.024}$	$205.5_{\pm161.5}$
		CopulaCPTS	$1.0_{\pm.000}$	$22.3_{\pm19.0}$	$1.0_{\pm.000}$	$611.3_{\pm484.7}$	$1.0_{\pm.000}$	$3.50 \times 10^5_{\pm3.73\times10^5}$
		OT-CP	$0.964_{\pm.015}$	$2.71_{\pm1.54}$	$0.958_{\pm.015}$	$42.3_{\pm38.4}$	$0.927_{\pm.027}$	$1.28 \times 10^2_{\pm713}$
		CONTRA	$0.979_{\pm.024}$	$32.9_{\pm25.8}$	$1.000_{\pm.000}$	$7.89 \times 10^5_{\pm1.49\times10^6}$	$0.994_{\pm.006}$	$5.88 \times 10^{11}_{\pm1.16\times10^{12}}$
		Local Ellipsoid	$0.964_{\pm.015}$	$1.38_{\pm.419}$	$0.971_{\pm.013}$	$8.63_{\pm5.90}$	$0.974_{\pm.011}$	$394.9_{\pm522.4}$
		Empirical Copula	$0.951_{\pm.013}$	$1.22_{\pm.316}$	$0.958_{\pm.019}$	$4.94_{\pm2.57}$	$0.948_{\pm.012}$	$77.4_{\pm26.1}$
		Gaussian Copula	$0.945_{\pm.017}$	$1.17_{\pm.289}$	$0.958_{\pm.019}$	$5.11_{\pm2.40}$	$0.948_{\pm.012}$	$77.4_{\pm26.1}$
		TFT	$0.723_{\pm.172}$	$1.34_{\pm.588}$	$0.515_{\pm.174}$	$4.26_{\pm3.52}$	$0.187_{\pm.126}$	$6.75_{\pm3.19}$
		DeepAR	$0.909_{\pm.036}$	$1.32_{\pm.445}$	$0.672_{\pm.130}$	$4.84_{\pm3.86}$	$0.320_{\pm.160}$	$52.8_{\pm64.5}$
	LSTM	FCP	$0.952_{\pm.054}$	$\mathbf{1.18}_{\pm.215}$	$0.957_{\pm.022}$	$\mathbf{10.8}_{\pm1.05}$	$0.953_{\pm.056}$	$\mathbf{2.48 \times 10^3}_{\pm669}$
		MultiDimSPCI	$0.974_{\pm.009}$	$3.79_{\pm1.71}$	$0.926_{\pm.045}$	$63.9_{\pm58.4}$	$0.896_{\pm.035}$	$5.53 \times 10^3_{\pm6.31\times10^3}$
		CopulaCPTS	$1.0_{\pm.000}$	$45.7_{\pm45.4}$	$1.0_{\pm.000}$	$4.82 \times 10^3_{\pm3.73\times10^3}$	$1.0_{\pm.000}$	$2.83 \times 10^7_{\pm3.28\times10^7}$
		OT-CP	$0.970_{\pm.033}$	$9.13_{\pm4.88}$	$0.939_{\pm.052}$	$212.3_{\pm124.5}$	$0.943_{\pm.053}$	$8.39 \times 10^4_{\pm4.68\times10^4}$
		CONTRA	$0.826_{\pm.201}$	$0.317_{\pm.222}$	$0.804_{\pm.178}$	$0.192_{\pm.124}$	$0.761_{\pm.205}$	$25.0_{\pm35.2}$
		Local Ellipsoid	$0.978_{\pm.043}$	$10.5_{\pm6.97}$	$1.0_{\pm.000}$	$354.4_{\pm406.8}$	$1.0_{\pm.000}$	$2.63 \times 10^5_{\pm2.70\times10^5}$
		Empirical Copula	$0.983_{\pm.035}$	$14.2_{\pm8.19}$	$1.0_{\pm.000}$	$494.5_{\pm196.1}$	$1.0_{\pm.000}$	$4.46 \times 10^5_{\pm9.82\times10^4}$
		Gaussian Copula	$0.983_{\pm.035}$	$14.1_{\pm8.18}$	$1.0_{\pm.000}$	$499.1_{\pm189.5}$	$1.0_{\pm.000}$	$5.24 \times 10^5_{\pm1.89\times10^5}$
		TFT	$0.550_{\pm.321}$	$1.90_{\pm.695}$	$0.395_{\pm.195}$	$3.93_{\pm2.01}$	$0.136_{\pm.189}$	$23.7_{\pm34.8}$
		DeepAR	$0.786_{\pm.065}$	$1.69_{\pm.489}$	$0.305_{\pm.258}$	$9.88_{\pm10.1}$	$0.00_{\pm.000}$	$22.8_{\pm32.6}$
Traffic	LOO Bootstrap	FCP	$0.957_{\pm.014}$	$\mathbf{0.915}_{\pm.119}$	$0.953_{\pm.009}$	$\mathbf{1.06}_{\pm.431}$	$0.965_{\pm.015}$	$\mathbf{1.53}_{\pm.161}$
		MultiDimSPCI	$0.963_{\pm.008}$	$1.58_{\pm.446}$	$0.968_{\pm.006}$	$2.62_{\pm.908}$	$0.971_{\pm.004}$	$10.7_{\pm4.60}$
		CopulaCPTS	$1.000_{\pm.000}$	$21.6_{\pm16.3}$	$1.000_{\pm.000}$	$645.8_{\pm645.5}$	$1.000_{\pm.000}$	$3.18 \times 10^5_{\pm4.80\times10^5}$
		OT-CP	$0.966_{\pm.008}$	$2.03_{\pm.685}$	$0.963_{\pm.007}$	$32.0_{\pm20.0}$	$0.954_{\pm.007}$	$3.90 \times 10^3_{\pm1.22\times10^3}$
		CONTRA	$0.950_{\pm.026}$	$1.32_{\pm.719}$	$0.953_{\pm.021}$	$1.58_{\pm1.06}$	$0.931_{\pm.036}$	$6.21_{\pm4.51}$
		Local Ellipsoid	$0.970_{\pm.007}$	$2.04_{\pm.505}$	$0.975_{\pm.005}$	$2.95_{\pm1.06}$	$0.980_{\pm.003}$	$3.82_{\pm1.13}$
		Empirical Copula	$0.973_{\pm.006}$	$2.35_{\pm.446}$	$0.972_{\pm.004}$	$5.61_{\pm1.48}$	$0.970_{\pm.005}$	$40.4_{\pm6.04}$
		Gaussian Copula	$0.973_{\pm.006}$	$2.37_{\pm.430}$	$0.972_{\pm.004}$	$5.61_{\pm1.48}$	$0.970_{\pm.005}$	$40.4_{\pm6.04}$
		TFT	$0.407_{\pm.065}$	$0.292_{\pm.089}$	$0.189_{\pm.306}$	$0.07_{\pm.031}$	$0.09_{\pm.007}$	$0.009_{\pm.007}$
		DeepAR	$0.443_{\pm.095}$	$0.308_{\pm.088}$	$0.197_{\pm.054}$	$0.07_{\pm.030}$	$0.09_{\pm.028}$	$0.004_{\pm.003}$
	LSTM	FCP	$0.968_{\pm.022}$	$\mathbf{0.859}_{\pm.075}$	$0.966_{\pm.022}$	$\mathbf{1.05}_{\pm.111}$	$0.950_{\pm.010}$	$\mathbf{1.82}_{\pm.287}$
		MultiDimSPCI	$0.957_{\pm.007}$	$0.870_{\pm.383}$	$0.960_{\pm.009}$	$1.59_{\pm.588}$	$0.952_{\pm.014}$	$14.2_{\pm7.56}$
		CopulaCPTS	$1.000_{\pm.000}$	$21.9_{\pm12.7}$	$1.000_{\pm.000}$	$330.0_{\pm219.4}$	$0.992_{\pm.002}$	$4.47 \times 10^4_{\pm4.23\times10^4}$
		OT-CP	$0.953_{\pm.006}$	$0.920_{\pm.379}$	$0.939_{\pm.027}$	$11.8_{\pm9.35}$	$0.921_{\pm.029}$	$730.2_{\pm698.7}$
		CONTRA	$0.940_{\pm.258}$	$0.222_{\pm.082}$	$0.942_{\pm.028}$	$0.106_{\pm.056}$	$0.910_{\pm.032}$	$0.050_{\pm.050}$
		Local Ellipsoid	$0.957_{\pm.023}$	$0.987_{\pm.413}$	$0.948_{\pm.008}$	$1.48_{\pm.559}$	$0.928_{\pm.017}$	$3.37_{\pm.605}$
		Empirical Copula	$0.955_{\pm.005}$	$3.81_{\pm.629}$	$0.948_{\pm.010}$	$25.8_{\pm5.06}$	$0.920_{\pm.017}$	$1.22 \times 10^3_{\pm281.9}$
		Gaussian Copula	$0.953_{\pm.006}$	$3.74_{\pm.570}$	$0.952_{\pm.011}$	$26.4_{\pm4.00}$	$0.920_{\pm.017}$	$1.22 \times 10^3_{\pm281.9}$
		TFT	$0.374_{\pm.110}$	$0.285_{\pm.106}$	$0.192_{\pm.048}$	$0.06_{\pm.022}$	$0.062_{\pm.015}$	$0.003_{\pm.002}$
		DeepAR	$0.386_{\pm.065}$	$0.266_{\pm.069}$	$0.211_{\pm.056}$	$0.06_{\pm.017}$	$0.09_{\pm.009}$	$0.003_{\pm.001}$
Solar	LOO Bootstrap	FCP	$0.957_{\pm.007}$	$\mathbf{1.48}_{\pm.292}$	$0.969_{\pm.003}$	$\mathbf{4.18}_{\pm.597}$	-	-
		MultiDimSPCI	$0.968_{\pm.005}$	$1.97_{\pm.076}$	$0.971_{\pm.003}$	$11.4_{\pm1.20}$	-	-
		CopulaCPTS	$1.000_{\pm.000}$	$67.9_{\pm12.6}$	$1.000_{\pm.000}$	$7.25 \times 10^3_{\pm1.86\times10^3}$	-	-
		OT-CP	$0.984_{\pm.004}$	$3.69_{\pm.797}$	$0.971_{\pm.006}$	$248.9_{\pm40.3}$	-	-
		CONTRA	$0.950_{\pm.012}$	$3.08_{\pm.584}$	$0.936_{\pm.013}$	$30.8_{\pm16.7}$	-	-
		Local Ellipsoid	$0.947_{\pm.004}$	$1.44_{\pm.188}$	$0.948_{\pm.005}$	$1.87_{\pm.540}$	-	-
		Empirical Copula	$0.986_{\pm.004}$	$4.47_{\pm.174}$	$0.988_{\pm.004}$	$36.5_{\pm4.03}$	-	-
		Gaussian Copula	$0.986_{\pm.004}$	$4.47_{\pm.174}$	$0.989_{\pm.003}$	$38.2_{\pm1.37}$	-	-
		TFT	$0.782_{\pm.026}$	$0.779_{\pm.056}$	$0.722_{\pm.028}$	$3.18_{\pm.415}$	-	-
		DeepAR	$0.802_{\pm.121}$	$1.03_{\pm.114}$	$0.713_{\pm.086}$	$6.73_{\pm1.09}$	-	-
	LSTM	FCP	$0.968_{\pm.009}$	$\mathbf{1.16}_{\pm.092}$	$0.961_{\pm.008}$	$\mathbf{2.09}_{\pm.566}$	-	-
		MultiDimSPCI	$0.969_{\pm.004}$	$1.31_{\pm.010}$	$0.976_{\pm.005}$	$6.46_{\pm2.51}$	-	-
		CopulaCPTS	$1.000_{\pm.000}$	$44.8_{\pm9.88}$	$1.000_{\pm.000}$	$3.34 \times 10^3_{\pm570}$	-	-
		OT-CP	$0.979_{\pm.005}$	$2.25_{\pm.247}$	$0.963_{\pm.008}$	$142.0_{\pm40.8}$	-	-
		CONTRA	$0.938_{\pm.012}$	$0.100_{\pm.026}$	$0.913_{\pm.013}$	$0.022_{\pm.014}$	-	-
		Local Ellipsoid	$0.972_{\pm.005}$	$1.27_{\pm.143}$	$0.978_{\pm.004}$	$2.43_{\pm.996}$	-	-
		Empirical Copula	$0.987_{\pm.002}$	$6.47_{\pm.103}$	$0.990_{\pm.003}$	$67.7_{\pm10.9}$	-	-
		Gaussian Copula	$0.992_{\pm.001}$	$7.11_{\pm.216}$	$0.997_{\pm.001}$	$89.9_{\pm4.69}$	-	-
		TFT	$0.746_{\pm.081}$	$0.651_{\pm.095}$	$0.684_{\pm.063}$	$1.63_{\pm.177}$	-	-
		DeepAR	$0.839_{\pm.028}$	$1.01_{\pm.088}$	$0.715_{\pm.043}$	$3.57_{\pm.493}$	-	-

where $\mathcal{D}_{\text{test}}$ denotes the test set. The average prediction set size is computed by averaging the sizes of $\hat{C}_i$ over the test set, with the specific definition of the set size depending on the geometric form of each method.

Results. Table 1 presents the results of experiments on three real-world datasets. FCP consistently obtained smaller prediction sets than all baselines while maintaining the target coverage. The performance gains of FCP were especially notable for higher outcome dimensions, showing significantly smaller prediction set sizes with lower variability. Moreover, FCP maintained stable coverage across varying d_y, whereas baseline methods often suffered from undercoverage or from overcoverage coupled with either overly contracted or excessively inflated prediction sets. In particular, methods relying on the exchangeability assumption often exhibited severe coverage errors and highly unstable prediction set sizes.

MultiDimSPCI and CP using local ellipsoids generally showed good performance. In particular, on the solar dataset, CP with local ellipsoids achieved performance comparable to FCP. This is possibly due to their ability to capture temporal or local correlations, respectively. OT-CP and CONTRA also performed well in certain experiments, indicating some potential to adapt beyond the exchangeability assumption. We observed that increasing the guidance scale w often reduced the prediction set size, though at the cost of slightly lower coverage. In practice, an effective range for w was typically between 1 and 1.5 across our experiments.

Ablation study. We conduct an ablation study to assess the impact of the encoder. Specifically, we evaluate FCP with and without the encoder, where in the latter case the guidance h is replaced by the concatenation of the feature at time i and residual at time $i-1$. Table 2 reports the average empirical coverage and prediction set sizes of FCP with and without the encoder on the wind dataset. We observe that removing the encoder led to less stable coverage and noticeably larger prediction set sizes.

Since the conditional coverage bound of FCP relies on the bi-Lipschitz flow assumption (Assumption 4.6), we conduct an additional experiment using iResNet (Behrmann et al., 2019) to model the vector field, ensuring this assumption is satisfied. Table 7 reports the average empirical coverage and prediction set sizes of FCP with MLP and iResNet across the three datasets with varying d_y. We observe that imposing bi-Lipschitzness in the vector field did not negatively affect either coverage or prediction set size.

Table 2: Average empirical coverage and prediction set sizes obtained by FCP and FCP without the encoder on the wind dataset, evaluated under different base predictors and varying outcome dimensions d_y. The target confidence level was set to 0.95.

Base Predictor	Method	$\mathbf{d_y = 2}$		$\mathbf{d_y = 4}$		$\mathbf{d_y = 8}$	
		Coverage	**Size**	**Coverage**	**Size**	**Coverage**	**Size**
LOO Bootstrap	FCP with Encoder	$0.951_{\pm.018}$	$0.88_{\pm.089}$	$0.953_{\pm.006}$	$3.43_{\pm1.37}$	$0.956_{\pm.010}$	$19.4_{\pm10.2}$
	FCP w/o Encoder	$0.948_{\pm.023}$	$1.13_{\pm.193}$	$0.964_{\pm.005}$	$3.99_{\pm1.03}$	$0.964_{\pm.010}$	$35.3_{\pm14.0}$
LSTM	FCP with Encoder	$0.952_{\pm.054}$	$1.18_{\pm.215}$	$0.957_{\pm.022}$	$10.8_{\pm1.05}$	$0.953_{\pm.056}$	$2.48 \times 10^3_{\pm669}$
	FCP w/o Encoder	$0.965_{\pm.011}$	$1.92_{\pm.367}$	$0.957_{\pm.014}$	$12.2_{\pm15.0}$	$0.935_{\pm.007}$	$5.55 \times 10^3_{\pm7.47\times10^3}$

6 Conclusion

In this study, we proposed a novel conformal prediction method for multi-dimensional time series using flow with classifier-free guidance. We provided coverage guarantees of our method by establishing exact non-asymptotic marginal coverage and a finite-sample bound on conditional coverage. Experiments on real-world datasets with a broad set of baselines demonstrated that our method constructs smaller prediction sets while satisfying the target coverage, consistently outperforming the baselines. Future work will investigate dynamic optimal transport mappings, implemented through flow, between the non-conformity scores and the source distribution, with the aim of constructing more efficient prediction sets and deriving sharper coverage bounds.

Ethics Statement

We confirm that our study complies with the ICLR Code of Ethics and does not present additional ethical issues.

Reproducibility Statement

The source code for the method and experiments will be made publicly available. Detailed descriptions of the experimental setup, including hyperparameters, datasets, and implementation, are provided in the Experiments section and the Appendix for reproducibility.

References

Anastasios N Angelopoulos and Stephen Bates. A gentle introduction to conformal prediction and distribution-free uncertainty quantification. *arXiv preprint arXiv:2107.07511*, 2021.

Andreas Auer, Martin Gauch, Daniel Klotz, and Sepp Hochreiter. Conformal prediction for time series with modern hopfield networks. *Advances in Neural Information Processing Systems*, 36, 2024.

Rina Foygel Barber, Emmanuel J Candes, Aaditya Ramdas, and Ryan J Tibshirani. Conformal prediction beyond exchangeability. *The Annals of Statistics*, 51(2):816–845, 2023.

Jens Behrmann, Will Grathwohl, Ricky TQ Chen, David Duvenaud, and Jörn-Henrik Jacobsen. Invertible residual networks. In *International conference on machine learning*, pp. 573–582. PMLR, 2019.

Peter J Bickel, Ya'acov Ritov, and Alexandre B Tsybakov. Simultaneous analysis of lasso and dantzig selector. 2009.

Stéphane Boucheron, Gábor Lugosi, and Olivier Bousquet. Concentration inequalities. In *Summer school on machine learning*, pp. 208–240. Springer, 2003.

George EP Box, Gwilym M Jenkins, Gregory C Reinsel, and Greta M Ljung. *Time series analysis: forecasting and control*. John Wiley & Sons, 2015.

Sacha Braun, Liviu Aolaritei, Michael I Jordan, and Francis Bach. Minimum volume conformal sets for multivariate regression. *arXiv preprint arXiv:2503.19068*, 2025.

Ricky TQ Chen, Jens Behrmann, David K Duvenaud, and Jörn-Henrik Jacobsen. Residual flows for invertible generative modeling. *Advances in neural information processing systems*, 32, 2019.

Xiaohong Chen and Halbert White. Improved rates and asymptotic normality for nonparametric neural network estimators. *IEEE Transactions on Information Theory*, 45(2):682–691, 1999.

Victor Chernozhukov, Alfred Galichon, Marc Hallin, and Marc Henry. Monge-kantorovich depth, quantiles, ranks and signs. *Annals of Statistics*, 45(1):223–256, 2017.

Prafulla Dhariwal and Alexander Nichol. Diffusion models beat gans on image synthesis. *Advances in neural information processing systems*, 34:8780–8794, 2021.

John R Dormand and Peter J Prince. A family of embedded runge-kutta formulae. *Journal of computational and applied mathematics*, 6(1):19–26, 1980.

Aryeh Dvoretzky, Jack Kiefer, and Jacob Wolfowitz. Asymptotic minimax character of the sample distribution function and of the classical multinomial estimator. *The Annals of Mathematical Statistics*, pp. 642–669, 1956.

Patrick Esser, Sumith Kulal, Andreas Blattmann, Rahim Entezari, Jonas Müller, Harry Saini, Yam Levi, Dominik Lorenz, Axel Sauer, Frederic Boesel, et al. Scaling rectified flow transformers for high-resolution image synthesis. In *Forty-first international conference on machine learning*, 2024.

Zhenhan Fang, Aixin Tan, and Jian Huang. CONTRA: Conformal prediction region via normalizing flow transformation. In *The Thirteenth International Conference on Learning Representations*, 2025. URL https://openreview.net/forum?id=pOO9cqLq7Q.

Thomas Hakon Gronwall. Note on the derivatives with respect to a parameter of the solutions of a system of differential equations. *Annals of Mathematics*, 20(4):292–296, 1919.

Marc Hallin, Eustasio del Barrio, Juan Cuesta-Albertos, and Carlos Matrán. Distribution and quantile functions, ranks and signs in dimension d: A measure transportation approach. *Annals of statistics*, 49(2):1139–1165, 2021.

Iain Henderson, Adrien Mazoyer, and Fabrice Gamboa. Adaptive inference with random ellipsoids through conformal conditional linear expectation. *arXiv preprint arXiv:2409.18508*, 2024.

Morris W Hirsch, Stephen Smale, and Robert L Devaney. *Differential equations, dynamical systems, and an introduction to chaos*. Academic press, 2013.

Jonathan Ho and Tim Salimans. Classifier-free diffusion guidance. *arXiv preprint arXiv:2207.12598*, 2022.

Sepp Hochreiter and Jürgen Schmidhuber. Long short-term memory. *Neural computation*, 9(8): 1735–1780, 1997.

Chancellor Johnstone and Eugene Ndiaye. Exact and approximate conformal inference in multiple dimensions. *arXiv preprint arXiv:2210.17405*, 2022.

Jongseon Kim, Hyungjoon Kim, HyunGi Kim, Dongjun Lee, and Sungroh Yoon. A comprehensive survey of deep learning for time series forecasting: architectural diversity and open challenges. *Artificial Intelligence Review*, 58(7):1–95, 2025.

Diederik P Kingma. Adam: A method for stochastic optimization. *arXiv preprint arXiv:1412.6980*, 2014.

Michal Klein, Louis Bethune, Eugene Ndiaye, and Marco Cuturi. Multivariate conformal prediction using optimal transport. *arXiv preprint arXiv:2502.03609*, 2025.

Michael R Kosorok. *Introduction to empirical processes and semiparametric inference*, volume 61. Springer, 2008.

Bryan Lim, Sercan Ö Arık, Nicolas Loeff, and Tomas Pfister. Temporal fusion transformers for interpretable multi-horizon time series forecasting. *International Journal of Forecasting*, 37(4): 1748–1764, 2021.

Yaron Lipman, Ricky TQ Chen, Heli Ben-Hamu, Maximilian Nickel, and Matt Le. Flow matching for generative modeling. *arXiv preprint arXiv:2210.02747*, 2022.

Soundouss Messoudi, Sébastien Destercke, and Sylvain Rousseau. Copula-based conformal prediction for multi-target regression. *Pattern Recognition*, 120:108101, 2021.

Soundouss Messoudi, Sébastien Destercke, and Sylvain Rousseau. Ellipsoidal conformal inference for multi-target regression. In *Conformal and Probabilistic Prediction with Applications*, pp. 294–306. PMLR, 2022.

John A Miller, Mohammed Aldosari, Farah Saeed, Nasid Habib Barna, Subas Rana, I Budak Arpinar, and Ninghao Liu. A survey of deep learning and foundation models for time series forecasting. *arXiv preprint arXiv:2401.13912*, 2024.

J.R. Munkres. *Topology*. Featured Titles for Topology. Prentice Hall, Incorporated, 2000. ISBN 9780131816299. URL https://books.google.com/books?id=XjoZAQAAIAAJ.

Art B. Owen. *Practical Quasi-Monte Carlo Integration*. https://artowen.su.domains/mc/practicalqmc.pdf, 2023.

Adam Polyak, Amit Zohar, Andrew Brown, Andros Tjandra, Animesh Sinha, Ann Lee, Apoorv Vyas, Bowen Shi, Chih-Yao Ma, Ching-Yao Chuang, David Yan, Dhruv Choudhary, Dingkang Wang, Geet Sethi, Guan Pang, Haoyu Ma, Ishan Misra, Ji Hou, Jialiang Wang, Kiran Jagadeesh, Kunpeng Li, Luxin Zhang, Mannat Singh, Mary Williamson, Matt Le, Matthew Yu, Mitesh Kumar Singh, Peizhao Zhang, Peter Vajda, Quentin Duval, Rohit Girdhar, Roshan Sumbaly, Sai Saketh Rambhatla, Sam Tsai, Samaneh Azadi, Samyak Datta, Sanyuan Chen, Sean Bell, Sharadh Ramaswamy, Shelly Sheynin, Siddharth Bhattacharya, Simran Motwani, Tao Xu, Tianhe Li, Tingbo Hou, Wei-Ning Hsu, Xi Yin, Xiaoliang Dai, Yaniv Taigman, Yaqiao Luo, Yen-Cheng Liu, Yi-Chiao Wu, Yue Zhao, Yuval Kirstain, Zecheng He, Zijian He, Albert Pumarola, Ali Thabet, Artsiom Sanakoyeu, Arun Mallya, Baishan Guo, Boris Araya, Breena Kerr, Carleigh Wood, Ce Liu, Cen Peng, Dimitry Vengertsev, Edgar Schonfeld, Elliot Blanchard, Felix Juefei-Xu, Fraylie Nord, Jeff Liang, John Hoffman, Jonas Kohler, Kaolin Fire, Karthik Sivakumar, Lawrence Chen, Licheng Yu, Luya Gao, Markos Georgopoulos, Rashel Moritz, Sara K. Sampson, Shikai Li, Simone Parmeggiani, Steve Fine, Tara Fowler, Vladan Petrovic, and Yuming Du. Movie gen: A cast of media foundation models, 2025. URL https://arxiv.org/abs/2410.13720.

Emmanuel Rio et al. *Asymptotic theory of weakly dependent random processes*, volume 80. Springer, 2017.

David Salinas, Valentin Flunkert, Jan Gasthaus, and Tim Januschowski. Deepar: Probabilistic forecasting with autoregressive recurrent networks. *International journal of forecasting*, 36(3):1181–1191, 2020.

Glenn Shafer and Vladimir Vovk. A tutorial on conformal prediction. *Journal of Machine Learning Research*, 9(3), 2008.

Ilya M Sobol. The distribution of points in a cube and the approximate evaluation of integrals. *USSR Computational mathematics and mathematical physics*, 7:86–112, 1967.

Yang Song, Jascha Sohl-Dickstein, Diederik P Kingma, Abhishek Kumar, Stefano Ermon, and Ben Poole. Score-based generative modeling through stochastic differential equations. *arXiv preprint arXiv:2011.13456*, 2020.

Kamile Stankeviciute, Ahmed M Alaa, and Mihaela van der Schaar. Conformal time-series forecasting. *Advances in neural information processing systems*, 34:6216–6228, 2021.

Sophia Sun and Rose Yu. Copula conformal prediction for multi-step time series forecasting. *arXiv preprint arXiv:2212.03281*, 2022.

Gauthier Thurin, Kimia Nadjahi, and Claire Boyer. Optimal transport-based conformal prediction. In *Forty-second International Conference on Machine Learning*, 2025.

Ryan J Tibshirani, Rina Foygel Barber, Emmanuel Candes, and Aaditya Ramdas. Conformal prediction under covariate shift. *Advances in neural information processing systems*, 32, 2019.

Renukanandan Tumu, Matthew Cleaveland, Rahul Mangharam, George Pappas, and Lars Lindemann. Multi-modal conformal prediction regions by optimizing convex shape templates. In *6th Annual Learning for Dynamics & Control Conference*, pp. 1343–1356. PMLR, 2024.

Ashish Vaswani, Noam Shazeer, Niki Parmar, Jakob Uszkoreit, Llion Jones, Aidan N Gomez, Łukasz Kaiser, and Illia Polosukhin. Attention is all you need. *Advances in neural information processing systems*, 30, 2017.

Vladimir Vovk, Alexander Gammerman, and Glenn Shafer. *Algorithmic learning in a random world*, volume 29. Springer, 2005.

Qingsong Wen, Tian Zhou, Chaoli Zhang, Weiqi Chen, Ziqing Ma, Junchi Yan, and Liang Sun. Transformers in time series: a survey. In *Proceedings of the Thirty-Second International Joint Conference on Artificial Intelligence*, pp. 6778–6786, 2023.

Chen Xu and Yao Xie. Conformal prediction interval for dynamic time-series. In *International Conference on Machine Learning*, pp. 11559–11569. PMLR, 2021a.

Chen Xu and Yao Xie. Conformal anomaly detection on spatio-temporal observations with missing data. *arXiv preprint arXiv:2105.11886*, 2021b.

Chen Xu and Yao Xie. Conformal prediction for time series. *IEEE Transactions on Pattern Analysis and Machine Intelligence*, 2023a.

Chen Xu and Yao Xie. Sequential predictive conformal inference for time series. In *International Conference on Machine Learning*, pp. 38707–38727. PMLR, 2023b.

Chen Xu, Hanyang Jiang, and Yao Xie. Conformal prediction for multi-dimensional time series by ellipsoidal sets. *arXiv preprint arXiv:2403.03850*, 2024.

Minghe Zhang, Chen Xu, Andy Sun, Feng Qiu, and Yao Xie. Solar radiation ramping events modeling using spatio-temporal point processes. *arXiv preprint arXiv:2101.11179*, 2021. Accepted at the 2021 INFORMS Conference on Service Science (ICSS 2021).

Shixiang Zhu, Hanyu Zhang, Yao Xie, and Pascal Van Hentenryck. Multi-resolution spatio-temporal prediction with application to wind power generation. *arXiv preprint arXiv:2108.13285*, 2021.

A PROOFS

Proposition A.1. *Let $u_{t|x_1}(x \mid x_1)$ be the vector field generating the probability path $p_{t|x_1}(x \mid x_1)$. Then, the vector field $u_{t|h}(x \mid h)$ is a valid vector field generating $p_{t|h}(x \mid h)$.*

Proof. Since $u_{t|x_1}(x \mid x_1)$ generates the probability path $p_{t|x_1}(x \mid x_1)$, the continuity equation holds for each x_1:

$$\frac{\partial p_{t|x_1}(x \mid x_1)}{\partial t} + \text{div}\left(u_{t|x_1}(x \mid x_1) p_{t|x_1}(x \mid x_1)\right) = 0. \tag{26}$$

The time derivative of $p_{t|h}(x \mid h)$ is:

$$\begin{aligned}
\frac{\partial p_{t|h}(x \mid h)}{\partial t} &= \frac{\partial}{\partial t} \int p_{t|x_1}(x \mid x_1) q(x_1 \mid h)\, dx_1 \\
&= \int \frac{\partial p_{t|x_1}(x \mid x_1)}{\partial t} q(x_1 \mid h)\, dx_1 \\
&= -\int \text{div}\left(u_{t|x_1}(x \mid x_1) p_{t|x_1}(x \mid x_1)\right) q(x_1 \mid h)\, dx_1 \\
&= -\text{div}\left(\int u_{t|x_1}(x \mid x_1) p_{t|x_1}(x \mid x_1) q(x_1 \mid h)\, dx_1\right).
\end{aligned} \tag{27}$$

Since the marginal guided vector field is defined as:

$$u_{t|h}(x \mid h) := \int u_{t|x_1}(x \mid x_1) \frac{p_{t|x_1}(x \mid x_1) q(x_1 \mid h)}{p_{t|h}(x \mid h)}\, dx_1, \tag{28}$$

we can rewrite as:

$$u_{t|h}(x \mid h) p_{t|h}(x \mid h) = \int u_{t|x_1}(x \mid x_1) p_{t|x_1}(x \mid x_1) q(x_1 \mid h)\, dx_1. \tag{29}$$

Substituting equation (29) into equation (27), we have:

$$\frac{\partial p_{t|h}(x \mid h)}{\partial t} = -\text{div}\left(u_{t|h}(x \mid h) p_{t|h}(x \mid h)\right), \tag{30}$$

which is the continuity equation for $p_{t|h}(x \mid h)$ under the vector field $u_{t|h}(x \mid h)$. Therefore, $u_{t|h}(x \mid h)$ is a valid vector field generating $p_{t|h}(x \mid h)$. □

Proposition A.2. *With a given Gaussian probability path $p_{t|x_1}(x \mid x_1) = \mathcal{N}(x \mid \alpha_t x_1, \sigma_t^2 I_d)$, the guided vector field $u_{t|h}(x \mid h)$ can be reformulated as:*

$$u_{t|h}(x \mid h) = u_t(x) + b_t \nabla_x \log p_{h|t}(h \mid x). \tag{31}$$

Proof. By the definition of the guided marginal probability path:

$$p_{t|h}(x \mid h) = \int p_{t|x_1}(x \mid x_1) q(x_1 \mid h) dx_1, \tag{32}$$

where $p_{t|x_1}(x \mid x_1) = \mathcal{N}(x \mid \alpha_t x_1, \sigma_t^2 I)$. We express the score function as

$$\nabla_x \log p_{t|h}(x \mid h) = \frac{\nabla_x p_{t|h}(x \mid h)}{p_{t|h}(x \mid h)} \tag{33}$$

$$= \frac{\int \nabla_x p_{t|x_1}(x \mid x_1) q(x_1 \mid y) dx_1}{p_{t|h}(x \mid h)} \tag{34}$$

$$= \int \nabla_x \log p_{t|x_1}(x \mid x_1) \frac{p_{t|x_1}(x \mid x_1) q(x_1 \mid y)}{p_{t|h}(x \mid h)} dx_1. \tag{35}$$

Since $p_{t|x_1}(x \mid x_1) = \mathcal{N}(x \mid \alpha_t x_1, \sigma_t^2 I)$, we have:

$$u_t(x \mid x_1) = \frac{\dot{\alpha}_t}{\sigma_t}(x - \alpha_t x_1) + \dot{\alpha}_t x_1 \tag{36}$$

$$= \frac{\dot{\alpha}_t}{\sigma_t} x - \frac{\dot{\alpha}_t}{\sigma_t} \alpha_t x_1 + \dot{\alpha}_t x_1 \tag{37}$$

$$= \frac{\dot{\alpha}_t}{\sigma_t} x + (\dot{\alpha}_t - \frac{\dot{\alpha}_t}{\sigma_t} \alpha_t) x_1 \tag{38}$$

$$= \frac{\dot{\alpha}_t}{\alpha_t} x + (\dot{\alpha}_t \sigma_t - \alpha_t \dot{\sigma}_t) \frac{1}{\alpha_t \sigma_t}(x - \alpha_t x_1) \tag{39}$$

$$= \frac{\dot{\alpha}_t}{\alpha_t} x + (\dot{\alpha}_t \sigma_t - \alpha_t \dot{\sigma}_t) \frac{\sigma_t}{\alpha_t} \nabla \log p_t(x \mid x_1), \tag{40}$$

where $\dot{\alpha}_t$ denotes $\frac{d}{dt}\alpha_t$, and $\dot{\sigma}_t$ denotes $\frac{d}{dt}\sigma_t$. The last equality holds since $\nabla_x \log p_{t|x_1}(x \mid x_1) = -\frac{1}{\sigma_t^2}(x - \alpha_t x_1)$.

The guided velocity field is defined as:

$$u_{t|h}(x \mid h) = \int u_{t|x_1}(x \mid x_1) \frac{p_{t|x_1}(x \mid x_1) q(x_1 \mid h)}{p_{t|h}(x \mid h)} dx_1. \tag{41}$$

Therefore,

$$u_{t|h}(x \mid h) = a_t x + b_t \nabla_x \log p_t(x \mid h), \tag{42}$$

where $a_t = \frac{\dot{\alpha}_t}{\alpha_t}$, and $b_t = (\dot{\alpha}_t \sigma_t - \alpha_t \dot{\sigma}_t) \frac{\sigma_t}{\alpha_t}$.

By using the identity $\nabla_x \log p_{t|h}(x \mid h) = \nabla_x \log p_{h|t}(h \mid x) + \nabla_x \log p_t(x)$, we have:

$$u_t(x \mid h) = a_t x + b_t \left(\nabla \log p_{h|t}(h \mid x) + \nabla \log p_t(x)\right) = u_t(x) + b_t \nabla_x \log p_{h|t}(h \mid x). \tag{43}$$

□

Proposition A.3. *The log-determinant Jacobian ODE defined in equation equation 16 is equivalent to the divergence of the guided vector field.*

Proof. The Jacobian ODE is defined as:

$$\frac{d}{dt} J_{\psi_{t|h}}(x \mid h) = \frac{\partial u_{t|h}(\psi_{t|h}(x \mid h))}{\partial \psi_{t|h}(x \mid h)} \frac{\partial \psi_{t|h}(x \mid h)}{\partial x} = \frac{\partial u_{t|h}(\psi_{t|h}(x \mid h))}{\partial \psi_{t|h}(x \mid h)} J_{\psi_{t|h}}(x \mid h), \tag{44}$$

with the initial condition:

$$J_{\psi_{t=0|h}}(x \mid h) = I. \tag{45}$$

By using Jacobi's formula,

$$\frac{d}{dt} \det J_{\psi_{t|h}}(x \mid h) = \det J_{\psi_{t|h}}(x \mid h) \cdot \text{tr}\left(J^{-1}_{\psi_{t|h}}(x \mid h) \frac{d}{dt} J_{\psi_{t|h}}(x \mid h) \right). \tag{46}$$

Substituting equation equation 44 into equation equation 46, we obtain:

$$\frac{d}{dt} \det J_{\psi_{t|h}}(x \mid h) = \det J_{\psi_{t|h}}(x \mid h) \cdot \text{tr}\left(\frac{\partial u_{t|h}(\psi_{t|h}(x \mid h))}{\partial \psi_{t|h}(x \mid h)} \right). \tag{47}$$

Therefore,

$$\frac{d}{dt} \log |\det J_{\psi_{t|h}}(x \mid h)| = \text{tr}\left(\frac{\partial u_{t|h}(\psi_{t|h}(x \mid h))}{\partial \psi_{t|h}(x \mid h)} \right). \tag{48}$$

Since the trace of the Jacobian of a vector field corresponds to its divergence, we have:

$$\text{tr}\left(\frac{\partial u_{t|h}(\psi_{t|h}(x \mid h))}{\partial \psi_{t|h}(x \mid h)} \right) = \text{div}\left(u_{t|h}(\psi_{t|h}(x \mid h)) \right), \tag{49}$$

where $\text{div}(\cdot)$ denotes the divergence operator.

Therefore, the log-determinant of the Jacobian ODE is defined as:

$$\frac{d}{dt} \log |\det J_{\psi_{t|h}}(x \mid h)| = \text{div}\left(u_{t|h}(\psi_{t|h}(x \mid h)) \right) \tag{50}$$

with the initial condition:

$$\log |\det J_{\psi_{t=0|h}}(x \mid h)| = 0. \tag{51}$$

□

Theorem A.4 (Closed and connected sets under a continuous map, Munkres (2000))**.** *Let Z and Y be topological spaces, and let $\psi : Z \to Y$ be a continuous map. If $E \subset Z$ is closed and connected, then $\psi(E) \subset Y$ is also closed and connected.*

Assumption A.5 (Compact feature and outcome domains)**.** The feature and outcome domains are compact. That is, $x_i \in \mathcal{X} \subset \mathbb{R}^{d_x}$ and $y_i \in \mathcal{Y} \subset \mathbb{R}^{d_y}$, where $\mathcal{X}$ and $\mathcal{Y}$ are compact sets.

Remark A.6. While its not strictly required, further assume that the domains of x_i and y_i are compact, which ensures that the encoder output is also compact, as formalized in Assumption A.5. Under Assumption A.5, if the encoder is a continuous function that maps a sequence of inputs to a representation $h \in \mathbb{R}^{d_h}$, then the image of the encoder $\mathcal{H} \subset \mathbb{R}^{d_h}$ is compact.

Lemma A.7 (Lipschitz continuous of the guided flow)**.** *Let ψ_t denote the guided flow defined by a guided vector field u_t. If the guided vector field $u_t(x \mid h)$ is Lipschitz continuous in x uniformly over $t \in [0, 1]$ and $h \in \mathcal{H}$, i.e., there exists a constant $L_u > 0$ such that*

$$\|u_t(x \mid h) - u_t(x' \mid h)\| \leq L_u \|x - x'\| \quad \forall x, x', t, h, \tag{52}$$

then the guided flow $\psi_t(x \mid h)$ is Lipschitz continuous in x over $t \in [0, 1]$ and $h \in \mathcal{H}$. That is, there exists a constant $L_\psi > 0$ such that

$$\|\psi_t(x \mid h) - \psi_t(x' \mid h)\| \leq L_\psi \|x - x'\| \quad \forall x, x', t, h. \tag{53}$$

Proof. Let $d(t) = \|\psi_t(x \mid h) - \psi_t(x' \mid h)\|$

Since the guided vector field is Lipschitz continuous, there exists L_u such that

$$\|u_t(x \mid h) - u_t(x' \mid h)\| \leq L_u \|x - x'\|, \quad \forall t, h, x, x'. \tag{54}$$

This is equivalent to

$$\|u_t(\psi_t(x \mid h) \mid h) - u_t(\psi_t(x' \mid h) \mid h)\| \leq L_u \|\psi_t(x \mid h) - \psi_t(x' \mid h)\|, \quad \forall t, h, x, x'. \tag{55}$$

Let $z(t) = \psi_t(x \mid h) - \psi_t(x' \mid h)$, then

$$\frac{d}{dt} d(t) = \frac{1}{\|z(t)\|} \langle z(t), \frac{d}{dt} z(t) \rangle = \langle \frac{z(t)}{\|z(t)\|}, \frac{d}{dt} z(t) \rangle \tag{56}$$

Since $\frac{d}{dt} z(t) = u_t(\psi_t(x \mid h) \mid h) - u_t(\psi_t(x' \mid h) \mid h)$, by Cauchy-Schwarz inequality,

$$|\langle \frac{z(t)}{\|z(t)\|}, \frac{d}{dt} z(t) \rangle| \leq \|u_t(\psi_t(x \mid h) \mid h) - u_t(\psi_t(x' \mid h) \mid h)\| \tag{57}$$

Therefore,

$$\frac{d}{dt} d(t) \leq \|u_t(\psi_t(x \mid h) \mid h) - u_t(\psi_t(x' \mid h) \mid h)\| \tag{58}$$

Since the guided vector field is Lipschitz continuous,

$$\frac{d}{dt} d(t) \leq L_u d(t) \tag{59}$$

Based on Gronwall's inequality Gronwall (1919); Hirsch et al. (2013),

Assuming that $d(t) > 0$ divide both sides by $d(t)$. If $d(t) = 0$, the inequality holds.

$$\frac{1}{d(t)} \frac{d}{dt} d(t) \leq L \Rightarrow \frac{d}{dt} \log d(t) \leq L \tag{60}$$

Now integrate both sides from 0 to t:

$$\log d(t) - \log d(0) \leq Lt \Rightarrow \log \left(\frac{d(t)}{d(0)} \right) \leq Lt \Rightarrow \frac{d(t)}{d(0)} \leq e^{Lt} \Rightarrow d(t) \leq d(0) e^{Lt} \tag{61}$$

Since $d(0) = \|\psi_0(x \mid h) - \psi_0(x' \mid h)\| = \|x - x'\|$,

$$\|\psi_t(x \mid h) - \psi_t(x' \mid h)\| \leq e^{L_u t} \|x - x'\| \tag{62}$$

Therefore, we know that

$$\|\psi_t(x \mid h) - \psi_t(x' \mid h)\| \leq e^{L_u} \|x - x'\| \quad \forall x, x', t, h \tag{63}$$

□

Proof of Lemma 4.3. Since the probability density function of $Y = \psi(X)$ is the push-forward of p_X, we have:

$$p_Y(y) = p_X(\psi^{-1}(y)) \left| \det J_{\psi^{-1}}(y) \right|, \tag{64}$$

where $\det A$ denotes the determinant of a square matrix A and $J_{\psi^{-1}}(y) = \frac{\partial \psi^{-1}(y)}{\partial y}$ is the Jacobian of ψ^{-1}. The probability mass of the transformed set $\mathcal{A}' = \psi(\mathcal{A})$ is:

$$\mathbb{P}(Y \in \mathcal{A}') = \int_{\mathcal{A}'} p_Y(y)\, dy. \tag{65}$$

Using the change-of-variables $y = \psi(x)$ with $dy = |\det J_\psi(x)| dx$, we have:

$$\int_{\mathcal{A}'} p_Y(y)\, dy = \int_{\mathcal{A}} p_Y(\psi(x)) \left| \det J_\psi(x) \right| \, dx. \tag{66}$$

Substituting from equation equation 64, we have:

$$\int_{\mathcal{A}} p_Y(\psi(x)) \left|\det J_\psi(x)\right| \, dx = \int_{\mathcal{A}} p_X(x) \left|\det J_{\psi^{-1}}(\psi(x))\right| \left|\det J_\psi(x)\right| dx. \tag{67}$$

Since $J_{\psi^{-1}}(\psi(x)) = J_\psi(x)^{-1}$, we know that $|\det J_{\psi^{-1}}(\psi(x))| \cdot |\det J_\psi(x)| = 1$. Hence,

$$\int_{\mathcal{A}'} p_Y(y)\, dy = \int_{\mathcal{A}} p_X(x)\, dx. \tag{68}$$

□

Lemma A.8 (bi-Lipschitz guided flow)**.** *Assume that the guided vector field is bi-Lipschitz uniformly in x over $t \in [0,1]$ and $h \in \mathcal{H}$, i.e., there exists L_u and l_u such that*

$$l_u\|x - x'\| \le \|u_t(x \mid h) - u_t(x' \mid h)\| \le L_u\|x - x'\| \quad \forall t, h, x, x'. \tag{69}$$

Then the guided flow ψ is bi-Lipschitz. There exists L_ψ and l_ψ such that

$$l_\psi\|x - x'\| \le \|\psi_t(x \mid h) - \psi_t(x' \mid h)\| \le L_\psi\|x - x'\| \quad \forall t, h, x, x'. \tag{70}$$

Proof. Proof follows similarly to Lemma A.7. The upper Lipschitz bound follows from Lemma A.7. Let $z(t) = \psi_t(x \mid h) - \psi_t(x' \mid h)$ and $d(t) = \|\psi_t(x \mid h) - \psi_t(x' \mid h)\| = \|z_t\|$.

$$\frac{d}{dt}\|z(t)\|^2 = 2\langle z(t), \frac{d}{dt}z(t)\rangle \tag{71}$$

By Cauchy-Schwarz inequality,

$$\frac{d}{dt}\|z(t)\|^2 = \frac{d}{dt}d(t)^2 \ge -2\|z(t)\|\|\frac{d}{dt}z(t)\| \tag{72}$$

Since $\frac{d}{dt}z(t) = u_t(x \mid h) - u_t(x' \mid h)$ and $\|u_t(x \mid h) - u_t(x' \mid h)\| \ge l_u\|x - x'\| = l_u\|\psi_t(x \mid h) - \psi_t(x' \mid h)\|$, we obtain

$$\frac{d}{dt}d(t)^2 \ge -2l_u\|z(t)\|^2 = -2l_u d(t)^2 \tag{73}$$

Using Gronwall's inequality,

$$\|\psi_t(x \mid h) - \psi_t(x' \mid h)\| \ge e^{-l_u t}\|x - x'\| \tag{74}$$

Therefore, we know that

$$\|\psi_t(x \mid h) - \psi_t(x' \mid h)\| \ge e^{-l_u}\|x - x'\| \quad \forall x, x', t, h \tag{75}$$

Combining with the upper Lipschitz bound, we get

$$e^{-l_u}\|x - x'\| \le \|\psi_t(x \mid h) - \psi_t(x' \mid h)\| \le e^{L_u}\|x - x'\| \quad \forall x, x', t, h \tag{76}$$

□

Lemma A.9. *Under Assumption 4.8, $F_e(e_{T+1}) \sim \mathrm{Unif}[0,1]$.*

Proof. Since F_e is strictly increasing and continuous under Assumption 4.8, the Lemma holds for $e_{T+1} \sim F_e$. □

Lemma A.10 (Convergence of empirical CDF of i.i.d. $\{e_i\}_{i=1}^T$)**.** *Under Assumption 4.5 and 4.6, for any T, there exists an event A_T with probability at least $1 - \sqrt{\frac{\log(16T)}{T}}$, such that conditioned on A_T,*

$$\sup_x \left|\tilde{F}_{T+1}(x) - F_e(x)\right| \le \sqrt{\frac{\log(16T)}{T}}. \tag{77}$$

Proof of Lemma A.10. The proof follows the proof of Lemma 1 in Xu & Xie (2023a). Under the assumption that $\{e_i\}_{i=1}^{T+1}$ are i.i.d., the Dvoretzky–Kiefer–Wolfowitz (DKW) inequality (Dvoretzky et al., 1956; Kosorok, 2008) implies:

$$\mathbb{P}\left(\sup_x \left|\tilde{F}_{T+1}(x) - F_e(x)\right| > s_T\right) \leq 2e^{-2Ts_T^2}. \tag{78}$$

Choose $s_T = \sqrt{W(16T)/(2\sqrt{T})}$, where $W(T)$ denotes the Lambert W function satisfying $W(T)e^{W(T)} = T$. Since $W(16T) \leq \log(16T)$, it follows that $s_T \leq \sqrt{\log(16T)/T}$. Define the event A_T on which $\sup_x \left|\tilde{F}_{T+1}(x) - F_e(x)\right| \leq \sqrt{\log(16T)/T}$, so that we have:

$$\sup_x \left|\tilde{F}_{T+1}(x) - F_e(x)\right| \Big| A_T \leq \sqrt{\frac{\log(16T)}{T}}, \tag{79}$$

and

$$\mathbb{P}(A_T) > 1 - \sqrt{\frac{\log(16T)}{T}}. \tag{80}$$

□

Lemma A.11 (Gaussian concentration inequality, Theorem 5.6 in Boucheron et al. (2003))**.** *Let $X \sim \mathcal{N}(0, I_d)$ be a standard Gaussian random vector in $\mathbb{R}^d$ and let $f : \mathbb{R}^d \to \mathbb{R}$ be an L_f-Lipschitz continuous function. Then, for all $t > 0$,*

$$\mathbb{P}(f(X) \geq \mathbb{E}[f(X)] + t) \leq \exp\left(\frac{-t^2}{2{L_f}^2}\right), \tag{81}$$

Proposition A.12 (Gaussian concentration inequality with isotropic covariance)**.** *Let $X \sim \mathcal{N}(0, \gamma I_d)$ be an isotropic Gaussian random vector in $\mathbb{R}^d$ with covariance matrix $\gamma I_d \in \mathbb{R}^d$ for some $\gamma > 0$ and let $f : \mathbb{R}^d \to \mathbb{R}$ be an L_f-Lipschitz continuous function. Then, for all $t > 0$,*

$$\mathbb{P}(f(X) \geq \mathbb{E}[f(X)] + t) \leq \exp\left(\frac{-t^2}{2\gamma{L_f}^2}\right), \tag{82}$$

Proof. Let $X' \sim \mathcal{N}(0, I_d)$, and define $X = \sqrt{\gamma}X'$, so that $X \sim \mathcal{N}(0, \gamma I_d)$. Define the function $f_\gamma(x) := f(\sqrt{\gamma}x)$. Then f_γ is $\sqrt{\gamma}L_f$-Lipschitz. Applying Lemma A.11 to $f_\gamma(X')$, we obtain:

$$\mathbb{P}\left(f_\gamma(X') \geq \mathbb{E}[f_\gamma(X')] + t\right) \leq \exp\left(-\frac{t^2}{2\gamma L_f^2}\right). \tag{83}$$

Since $f(X) = f_\gamma(X')$,

$$\mathbb{P}(f(X) \geq \mathbb{E}[f(X)] + t) = \mathbb{P}\left(f_\gamma(X') \geq \mathbb{E}[f_\gamma(X')] + t\right) \leq \exp\left(-\frac{t^2}{2\gamma L_f^2}\right). \tag{84}$$

□

Lemma A.13 (Norm concentration of isotropic Gaussian random vectors)**.** *Let $X_i \sim \mathcal{N}(\boldsymbol{0}, \gamma I_d)$ be an isotropic Gaussian random vector in $\mathbb{R}^d$, and $\|\cdot\|$ be 2-norm. Then for any $\delta \in (0, 1)$, with probability at least $1 - \delta$, we have:*

$$\max_{1 \leq i \leq T} \|X_i\| \leq M_T, \tag{85}$$

where $M_T = \sqrt{\gamma}\left(\sqrt{d} + \sqrt{2\log(T/\delta)}\right)$.

Proof of Lemma A.13. Let $X \sim \mathcal{N}(0, \gamma I_d)$ be an isotropic Gaussian random vector in $\mathbb{R}^d$ with covariance matrix $\gamma I_d \in \mathbb{R}^d$ for some $\gamma > 0$ and let $f : \mathbb{R}^d \to \mathbb{R}$ be 2-norm, i.e., $f(X) = \|X\|$.

Using Proposition A.12 and since f is 1-Lipschitz continuous, we have for all $t > 0$:

$$\mathbb{P}(\|X\| \geq \mathbb{E}[\|X\|] + t) \leq \exp\left(-\frac{t^2}{2\gamma}\right). \tag{86}$$

Using Jensen's inequality and since $X \sim \mathcal{N}(0, \gamma I_d)$,

$$\mathbb{E}[\|X\|] \leq \sqrt{\mathbb{E}[\|X\|^2]} = \sqrt{\mathbb{E}[X^\top X]} = \sqrt{\mathrm{tr}(\gamma I_d)} = \sqrt{\gamma d}. \tag{87}$$

Therefore, for any $t > 0$,

$$\mathbb{P}\left(\|X\| \geq \sqrt{\gamma d} + t\right) \leq \exp\left(-\frac{t^2}{2\gamma}\right). \tag{88}$$

By the union bound,

$$\mathbb{P}\left(\max_{1\leq i\leq T} \|X_i\| \geq \sqrt{\gamma d} + t\right) \leq \sum_{i=1}^{T} \mathbb{P}\left(\|X_i\| \geq \sqrt{\gamma d} + t\right) \leq T \cdot \exp\left(-\frac{t^2}{2\gamma}\right). \tag{89}$$

By setting $T \cdot \exp\left(-t^2/2\gamma\right) \leq \delta$, we obtain:

$$t \geq \sqrt{2\gamma \log\left(\frac{T}{\delta}\right)}. \tag{90}$$

Therefore, with probability at least $1 - \delta$,

$$\max_{1\leq i\leq T} \|X_i\| \leq \sqrt{\gamma d} + \sqrt{2\gamma \log\left(\frac{T}{\delta}\right)}. \tag{91}$$

Defining $M_T := \sqrt{\gamma}\left(\sqrt{d} + \sqrt{2\log(T/\delta)}\right)$, we conclude:

$$\max_{1\leq i\leq T} \|X_i\| \leq M_T. \tag{92}$$

□

Lemma A.14 (Bound on the sum of differences between true and estimated non-conformity scores)**.** *Under Assumption 4.6 and 4.9, with probability at least* $1 - \delta$*,*

$$\sum_{i=1}^{T} |\hat{e}_i - e_i| \leq 2T(M_T L_{\psi^{-1}} \delta_T + L^2_{\psi^{-1}} \delta_T^2). \tag{93}$$

Proof. Since the encoder is fixed after convergence, it generates the same h for $\hat{\epsilon}$ and ϵ. Let $\hat{s}_i = \psi^{-1}(\hat{\epsilon}_i \mid h)$ and $s_i = \psi^{-1}(\epsilon_i \mid h)$.

Using the identity for the difference of squared norms:

$$\begin{aligned} \|\hat{s}_i\| &= \|s_i + (\hat{s}_i - s_i)\|^2 \\ &= \|s_i\|^2 + 2\langle s_i, \hat{s}_i - s_i\rangle + \|\hat{s}_i - s_i\|^2, \end{aligned} \tag{94}$$

we obtain:

$$\|\hat{s}_i\|^2 - \|s_i\|^2 = 2\langle s_i, \hat{s}_i - s_i\rangle + \|\hat{s}_i - s_i\|^2 \tag{95}$$

Therefore,

$$\begin{aligned} |\hat{e}_i - e_i| &= \left| \|\hat{s}_i\|^2 - \|s_i\|^2 \right| \\ &= \left| 2\langle s_i, \hat{s}_i - s_i \rangle + \|\hat{s}_i - s_i\|^2 \right|. \end{aligned} \tag{96}$$

By the Cauchy-Schwarz inequality,

$$|\langle s_i, \hat{s}_i - s_i \rangle| \leq \|s_i\| \cdot \|\hat{s}_i - s_i\|. \tag{97}$$

Since ψ^{-1} is Lipschitz continuous with Lipschitz constant $L_{\psi^{-1}}$, we have:

$$\|\hat{s}_i - s_i\| \leq L_{\psi^{-1}} \|\hat{\epsilon}_i - \epsilon_i\| = L_{\psi^{-1}} \|\Delta_i\|. \tag{98}$$

Substituting inequality (98) into the inner product bound in equation (97),

$$|\langle s_i, \hat{s}_i - s_i \rangle| \leq \|s_i\| \cdot \|\hat{s}_i - s_i\| \leq L_{\psi^{-1}} \|s_i\| \|\Delta_i\|. \tag{99}$$

Then, by the triangle inequality,

$$|\hat{e}_i - e_i| \leq 2L_{\psi^{-1}} \|s_i\| \|\Delta_i\| + L_{\psi^{-1}}^2 \|\Delta_i\|^2. \tag{100}$$

By Lemma A.13, we have with probability at least $1 - \delta$ that $\|s_i\| \leq M_T$ for all i, and by Assumption 4.9, $\|\Delta_i\| \leq \delta_T$. Substituting these into the inequality (100),

$$|\hat{e}_i - e_i| \leq 2M_T L_{\psi^{-1}} \delta_T + L_{\psi^{-1}}^2 \delta_T^2. \tag{101}$$

Summing over all $i = 1, \ldots, T$, we conclude:

$$\sum_{i=1}^{T} |\hat{e}_i - e_i| \leq T \left(2M_T L_{\psi^{-1}} \delta_T + L_{\psi^{-1}}^2 \delta_T^2 \right). \tag{102}$$

□

Lemma A.15 (Distance between the empirical CDF of $\{e_i\}_{i=1}^T$ and $\{\hat{e}_i\}_{i=1}^T$)**.** *Under Assumption 4.6, 4.8, and 4.9, with probability* $1 - \delta$*,* $\hat{F}_{T+1}(x)$ *and* $\tilde{F}_{T+1}(x)$ *satisfy*

$$\sup_x \left| \hat{F}_{T+1}(x) - \tilde{F}_{T+1}(x) \right| \leq (2L_{T+1} + 1) C_+ 2 \sup_x \left| \tilde{F}_{T+1}(x) - F_e(x) \right|, \tag{103}$$

where $C = \sqrt{M_T L_{\psi^{-1}} \delta_T + L_{\psi^{-1}}^2 \delta_T^2}$.

Proof of Lemma A.15. By Lemma A.14, we have with probability at least $1 - \delta$,

$$\sum_{t=1}^{T} |\hat{e}_t - e_t| \leq T \left(2M_T L_{\psi^{-1}} \delta_T + L_{\psi^{-1}}^2 \delta_T^2 \right). \tag{104}$$

Let $C = \left(2M_T L_{\psi^{-1}} \delta_T + L_{\psi^{-1}}^2 \delta_T^2 \right)^{1/2}$. Then,

$$\sum_{i=1}^{T} |\hat{e}_i - e_i| \leq TC^2. \tag{105}$$

Define $S = \{t : |\hat{e}_t - e_t| \geq C\}$. Then,

$$|S| \cdot C \leq \sum_{t=1}^{T} |\hat{e}_t - e_t| \leq TC^2, \tag{106}$$

which implies $|S| \leq TC$.

We can bound the difference between the empirical CDFs of $\hat{e}_i$ and e_i as follows:

$$\begin{aligned}
|\widehat{F}_{T+1}(x) - \widetilde{F}_{T+1}(x)| &\leq \frac{1}{T}\sum_{t=1}^{T} |\mathbb{1}\{\hat{e}_t \leq x\} - \mathbb{1}\{e_t \leq x\}| \\
&\leq \frac{1}{T}\left(|S| + \sum_{t\notin S} |\mathbb{1}\{\hat{e}_t \leq x\} - \mathbb{1}\{e_t \leq x\}|\right) \\
&\overset{(i)}{\leq} \frac{1}{T}\left(|S| + \sum_{t\notin S} \mathbb{1}\{|e_t - x| \leq C\}\right) \\
&\leq \frac{1}{T}\left(|S| + \sum_{t=1}^{T} \mathbb{1}\{|e_t - x| \leq C\}\right) \\
&\leq C + \mathbb{P}(|e_{T+1} - x| \leq C) \\
&\quad + \sup_x \left|\frac{1}{T}\sum_{t=1}^{T} \mathbb{1}\{|e_t - x| \leq C\} - \mathbb{P}(|e_{T+1} - x| \leq C)\right| \\
&\overset{(ii)}{=} C + [F_e(x+C) - F_e(x-C)] \\
&\quad + \sup_x \left|\left[\widetilde{F}_{T+1}(x+C) - \widetilde{F}_{T+1}(x-C)\right] - [F_e(x+C) - F_e(x-C)]\right| \\
&\overset{(iii)}{\leq} (2L_{T+1}+1)C + 2\sup_x |\widetilde{F}_{T+1}(x) - F_e(x)|.
\end{aligned} \tag{107}$$

Here, (i) follows from the inequality $|\mathbb{1}\{a \leq x\} - \mathbb{1}\{b \leq x\}| \leq \mathbb{1}\{|b - x| \leq |a - b|\}$ for $a, b \in \mathbb{R}$, (ii) follows from the identity $\mathbb{P}(|e_{T+1} - x| \leq C) = F_e(x + C) - F_e(x - C)$, and (iii) uses the Lipschitz continuity of $F_e(x)$.

□

Proof of Theorem 4.10. For any $\beta \in [0, \alpha]$,

$$\begin{aligned}
&\left|\mathbb{P}\left(Y_{T+1} \in \widehat{C}^{\alpha}_{T+1} \mid Z_{T+1} = z_{T+1}\right) - (1-\alpha)\right| \\
&= \left|\mathbb{P}\left(\hat{e}_{T+1} \in \left[\widehat{F}^{-1}_{T+1}(\beta),\, \widehat{F}^{-1}_{T+1}(1-\alpha+\beta)\right] \mid Z_{T+1} = z_{T+1}\right) - (1-\alpha)\right| \\
&\overset{(i)}{=} \left|\mathbb{P}\left(\beta \leq \widehat{F}_{T+1}(\hat{e}_{T+1}) \leq 1-\alpha+\beta\right) - \mathbb{P}\left(\beta \leq F_e(e_{T+1}) \leq 1-\alpha+\beta\right)\right|.
\end{aligned} \tag{108}$$

Equality (i) follows from Lemma A.9, which states that $F_e(e_{T+1}) \sim \mathrm{Unif}[0, 1]$. This can be further bounded by:

$$\begin{aligned}
&\left|\mathbb{P}\left(\beta \leq \widehat{F}_{T+1}(\hat{e}_{T+1}) \leq 1-\alpha+\beta\right) - \mathbb{P}\left(\beta \leq F_e(e_{T+1}) \leq 1-\alpha+\beta\right)\right| \\
&\leq \mathbb{E}\left|\mathbb{1}\left\{\beta \leq \widehat{F}_{T+1}(\hat{e}_{T+1}) \leq 1-\alpha+\beta\right\} - \mathbb{1}\left\{\beta \leq F_e(e_{T+1}) \leq 1-\alpha+\beta\right\}\right| \\
&\overset{(i)}{\leq} \mathbb{E}\left(\left|\mathbb{1}\left\{\beta \leq \widehat{F}_{T+1}(\hat{e}_{T+1})\right\} - \mathbb{1}\left\{\beta \leq F_e(e_{T+1})\right\}\right|\right. \\
&\qquad \left. + \left|\mathbb{1}\left\{\widehat{F}_{T+1}(\hat{e}_{T+1}) \leq 1-\alpha+\beta\right\} - \mathbb{1}\left\{F_e(e_{T+1}) \leq 1-\alpha+\beta\right\}\right|\right)
\end{aligned} \tag{109}$$

Here, inequality (i) follows from the fact that for any $a, b \in \mathbb{R}$ and real values $x, y \in \mathbb{R}$,

$$|\mathbb{1}\{a \leq x \leq b\} - \mathbb{1}\{a \leq y \leq b\}| \leq |\mathbb{1}\{a \leq x\} - \mathbb{1}\{a \leq y\}| + |\mathbb{1}\{x \leq b\} - \mathbb{1}\{y \leq b\}|. \tag{110}$$

By triangle inequality,

$$
\begin{aligned}
&\mathbb{E}\left(\left|\mathbb{1}\left\{\beta \le \widehat{F}_{T+1}(\hat{e}_{T+1})\right\} - \mathbb{1}\left\{\beta \le F_e(e_{T+1})\right\}\right|\right. \\
&\left. + \left|\mathbb{1}\left\{\widehat{F}_{T+1}(\hat{e}_{T+1}) \le 1-\alpha+\beta\right\} - \mathbb{1}\left\{F_e(e_{T+1}) \le 1-\alpha+\beta\right\}\right|\right) \\
&\le \underbrace{\mathbb{E}\left(\left|\mathbb{1}\{\beta \le \widehat{F}_{T+1}(\hat{e}_{T+1})\} - \mathbb{1}\{\beta \le F_e(e_{T+1})\}\right|\right)}_{(a)} \\
&+ \underbrace{\mathbb{E}\left(\left|\mathbb{1}\left\{\widehat{F}_{T+1}(\hat{e}_{T+1}) \le 1-\alpha+\beta\right\} - \mathbb{1}\left\{F_e(e_{T+1}) \le 1-\alpha+\beta\right\}\right|\right)}_{(b)}
\end{aligned} \tag{111}
$$

For term (a), we have:

$$
\begin{aligned}
&\mathbb{E}\left(\left|\mathbb{1}\{\beta \le \widehat{F}_{T+1}(\hat{e}_{T+1})\} - \mathbb{1}\{\beta \le F_e(e_{T+1})\}\right|\right) \\
&\le \mathbb{P}\left(|F_e(e_{T+1}) - \beta| \le |\widehat{F}_{T+1}(\hat{e}_{T+1}) - F_e(e_{T+1})|\right).
\end{aligned} \tag{112}
$$

This inequality follows from the fact that for $a, b \in \mathbb{R}$, $|\mathbb{1}\{a \le x\} - \mathbb{1}\{b \le x\}| \le \mathbb{1}\{|b-x| \le |a-b|\}$, and $\mathbb{E}[\mathbb{1}\{A\}] = \mathbb{P}(A)$.

Similarly, for term (b), we have:

$$
\begin{aligned}
&\mathbb{E}\left(\left|\mathbb{1}\left\{\widehat{F}_{T+1}(\hat{e}_{T+1}) \le 1-\alpha+\beta\right\} - \mathbb{1}\left\{F_e(e_{T+1}) \le 1-\alpha+\beta\right\}\right|\right) \\
&\le \mathbb{P}\left(|F_e(e_{T+1}) - (1-\alpha+\beta)| \le \left|\widehat{F}_{T+1}(\hat{e}_{T+1}) - F_e(e_{T+1})\right|\right).
\end{aligned} \tag{113}
$$

Therefore,

$$
\begin{aligned}
&\left|\mathbb{P}\left(Y_{T+1} \in \widehat{C}^{\alpha}_{T+1} \mid Z_{T+1} = z_{T+1}\right) - (1-\alpha)\right| \\
&\le \mathbb{P}\left(|F_e(e_{T+1}) - \beta| \le |\widehat{F}_{T+1}(\hat{e}_{T+1}) - F_e(e_{T+1})|\right) \\
&\quad + \mathbb{P}\left(|F_e(e_{T+1}) - (1-\alpha+\beta)| \le |\widehat{F}_{T+1}(\hat{e}_{T+1}) - F_e(e_{T+1})|\right)
\end{aligned} \tag{114}
$$

In Lemma A.10, we defined A_T as the event on which

$$
\sup_x |\tilde{F}_{T+1}(x) - F_e(x)| \big| A_T \le \sqrt{\frac{\log(16T)}{T}},
$$

where $\mathbb{P}(A_T) > 1 - \sqrt{\frac{\log(16T)}{T}}$. Let A_T^C denote the complement of the event A_T. For any $\gamma \in [0,1]$, we have:

$$
\begin{aligned}
&\mathbb{P}\left(|F_e(e_{T+1}) - \gamma| \le |\hat{F}_{T+1}(\hat{e}_{T+1}) - F_e(e_{T+1})|\right) \\
&\le \mathbb{P}\left(|F_e(e_{T+1}) - \gamma| \le |\hat{F}_{T+1}(\hat{e}_{T+1}) - F_e(e_{T+1})| \mid A_T\right) + \mathbb{P}(A_T^C) \\
&\le \mathbb{P}\Big(|F_e(e_{T+1}) - \gamma| \le |\hat{F}_{T+1}(\hat{e}_{T+1}) - F_e(\hat{e}_{T+1})| + |F_e(\hat{e}_{T+1}) - F_e(e_{T+1})| \,\Big|\, A_T\Big) \\
&\quad + \sqrt{\frac{\log(16T)}{T}}.
\end{aligned} \tag{115}
$$

To bound the conditional probability above, we note that with probability $1-\delta$, conditioning on the event A_T,

$$
\begin{aligned}
&|\widehat{F}_{T+1}(\hat{e}_{T+1}) - F_e(e_{T+1})| + |F_e(\hat{e}_{T+1}) - F_e(e_{T+1})| \,\big|\, A_T \\
&\overset{(i)}{\leq} \sup_x |\widehat{F}_{T+1}(x) - F_e(x)| \,\big|\, A_T + L_{T+1}|\hat{e}_{T+1} - e_{T+1}| \\
&\leq \sup_x |\widehat{F}_{T+1}(x) - \widetilde{F}_{T+1}(x)| \,\big|\, A_T + \sup_x |\widetilde{F}_{T+1}(x) - F_e(x)| \,\big|\, A_T + L_{T+1}|\hat{e}_{T+1} - e_{T+1}| \\
&\overset{(ii)}{\leq} (2L_{T+1}+1)C + 3\sup_x |\widetilde{F}_{T+1}(x) - F_e(x)| \,\big|\, A_T + L_{T+1}\delta_T \\
&\overset{(iii)}{\leq} 3\sqrt{\frac{\log(16T)}{T}} + \left(L_{T+1} + \frac{1}{2}\right)(2C + \delta_T).
\end{aligned} \tag{116}
$$

Here, inequality (i) holds due to the supremum of $|\widehat{F}_{T+1}(x) - F_e(x)|$ over x and Lipschitz continuity of F_e from Assumption 4.8. Inequality (ii) follows from Lemma A.15. Inequality (iii) follows from Lemma A.10.

Since $F_e(e_{T+1}) \sim \text{Unif}[0,1]$,

$$
\begin{aligned}
&\mathbb{P}\left(|F_e(e_{T+1}) - \gamma| \leq \left|\widehat{F}_{T+1}(\hat{e}_{T+1}) - F_e(\hat{e}_{T+1})\right| + |F_e(\hat{e}_{T+1}) - F_e(e_{T+1})| \,\middle|\, A_T\right) \\
&\leq 6\sqrt{\frac{\log(16T)}{T}} + 2\left(L_{T+1} + \frac{1}{2}\right)(2C + \delta_T).
\end{aligned} \tag{117}
$$

Therefore, by substituting inequality (117) to inequality (114), we obtain:

$$
\begin{aligned}
&\left|\mathbb{P}\left(Y_{T+1} \in \widehat{C}^{\alpha}_{T+1} \mid Z_{T+1} = z_{T+1}\right) - (1-\alpha)\right| \\
&\leq 12\sqrt{\frac{\log(16T)}{T}} + 4(L_{T+1} + \frac{1}{2})(2C + \delta_T).
\end{aligned} \tag{118}
$$

□

Definition A.16. A sequence of random variables $\{X_n\}$ is said to be *strictly stationary* if for every $k \geq 1$, any integers $n_1, \ldots, n_k$, and any integer h, the joint distribution of the random variables $(X_{n_1}, \ldots, X_{n_k})$ is the same as the joint distribution of $(X_{n_1+h}, \ldots, X_{n_k+h})$.

Definition A.17. A sequence of random variables $\{X_n\}$ is said to be *strongly mixing* (or α-*mixing*) if the mixing coefficients $\alpha(k)$ defined by

$$
\alpha(k) = \sup_{n \in \mathbb{N}} \sup_{A \in \mathcal{F}_1^n,\, B \in \mathcal{F}_{n+k}^{\infty}} |\mathbb{P}(A \cap B) - \mathbb{P}(A)\mathbb{P}(B)| \tag{119}
$$

satisfy $\alpha(k) \to 0$ as $k \to \infty$, where $\mathcal{F}_a^b$ denotes the σ-algebra generated by $\{X_a, \ldots, X_b\}$.

Lemma A.18 (Convergence of empirical CDF of stationary and strongly mixing $\{e_i\}_{i=1}^T$)**.** *Under Assumption 4.11, for any T, there exists an event A_T with probability at least $1 - (\frac{M(\log T)^2}{2T})^{1/3}$, such that conditioned on A_T,*

$$
\sup_x |\tilde{F}_{T+1}(x) - F_e(x)| \leq \frac{(\frac{M}{2})^{1/3}(\log T)^{2/3}}{T^{1/3}}. \tag{120}
$$

Proof of Lemma A.18. The proof follows similarly in the proof of Lemma B.11 in Xu et al. (2024). Define $v_T(x) := \sqrt{T}(\tilde{F}_{T+1}(x) - F_e(x))$. By using Proposition 7.1 in Rio et al. (2017), we have:

$$
\mathbb{E}\left(\sup_x |v_T(x)|^2\right) \leq \left(1 + 4\sum_{k=0}^{T} \alpha(k)\right)\left(3 + \frac{\log T}{2\log 2}\right)^2, \tag{121}
$$

where $\alpha(k)$ denotes the k-th mixing coefficient. Under Assumption 4.11, we have $\sum_{k\geq 0}\alpha(k) \leq M < \infty$. Applying Markov's inequality yields:

$$\mathbb{P}\left(\sup_x \left|\widetilde{F}_{T+1}(x) - F_e(x)\right| \geq s_T\right) \leq \frac{\mathbb{E}\left(\sup_x |v_T(x)|^2/T\right)}{s_T^2} \leq \frac{1+4M}{Ts_T^2}\left(3+\frac{\log T}{2\log 2}\right)^2. \quad (122)$$

By setting

$$s_T := \left(\frac{1+4M}{T}\left(3+\frac{\log T}{2\log 2}\right)^2\right)^{1/3} \approx \left(\frac{M(\log T)^2}{2T}\right)^{1/3}, \quad (123)$$

we then have:

$$\mathbb{P}\left(\sup_x \left|\widetilde{F}_{T+1}(x) - F_e(x)\right| \leq \left(\frac{M(\log T)^2}{2T}\right)^{1/3}\right) \geq 1 - \left(\frac{M(\log T)^2}{2T}\right)^{1/3}. \quad (124)$$

Define the event A_T on which $\sup_x \left|\tilde{F}_{T+1}(x) - F_e(x)\right| \leq \left(\frac{M(\log T)^2}{2T}\right)^{1/3}$, so that we have:

$$\sup_x \left|\tilde{F}_{T+1}(x) - F_e(x)\right| \Big| A_T \leq \left(\frac{M(\log T)^2}{2T}\right)^{1/3} \quad (125)$$

and

$$\mathbb{P}(A_T) > 1 - \left(\frac{M(\log T)^2}{2T}\right)^{1/3}. \quad (126)$$

□

Proof of Corollary 4.12. Under Assumption 4.11, the result follows by combining Lemma A.15 and A.18, using an argument analogous to the proof of Theorem 4.10.

□

B Experiment Details

B.1 Experiment Setup

OT-CP. We implemented OT-CP using the source code released by the authors Thurin et al. (2025). The training and validation sets were combined to form a calibration set. Following the setup in the original publication, 75% of the calibration set was used to solve OT, and the remaining 25% was used to calibrate the prediction sets.

CONTRA. As the source code from the original publication was not released, we implemented CONTRA ourselves following the methodology and details provided in Fang et al. (2025). Consistent with the original setup, we used six coupling layers with a hidden dimension of 128 and trained the model for 100 epochs with the same batch size as FCP and a learning rate of 0.001. The training and validation sets were combined into a calibration set, of which 50% was used to train the model and the remaining 50% was used to calibrate the prediction sets.

MultiDimSPCI. We implemented MultiDimSPCI using the source code released by the authors Xu et al. (2024). The context window size was set to 50 for all real-world datasets, consistent with the setup used for FCP. Following the original publication, the number of trees was set to 15. The training and validation sets were combined into a single training set.

Conformal prediction using copulas. We implemented this method using the source code released by the authors Messoudi et al. (2021), following the setup described in the original publication. The training and validation sets were combined to form a calibration set.

Conformal prediction using local ellipsoids We implemented this method using the source code provided by the authors Messoudi et al. (2022). Following the setup in the original publication, the training set was used as the proper training set and the validation set as the calibration set. The number of neighbors for kNN was set to 5% of the proper training set size, as suggested by the authors. We also experimented with different neighbor ratios, but these variations did not lead to meaningful differences in performance.

CopulaCPTS We implemented this method using the source code provided by the authors Sun & Yu (2022), following the setup described in the original publication. The training and validation sets were combined to form a calibration set.

Temporal Fusion Transformer We implemented Temporal Fusion Transformer (TFT) Lim et al. (2021) using `pytorch_forecasting`. A hyperparameter grid search was conducted on the training set of each dataset with $d_y = 2$ to determine the optimal configuration. We believe this hyperparameter search generalizes well to higher d_y within each dataset, since TFT makes predictions for each outcome dimension independently in our setup. Performance was observed to saturate at a model dimension of 32, with two attention heads and two layers, therefore these settings were used for all experiments. For consistency with FCP, the context window size was fixed at 50 across all experiments. We trained the models using the Adam optimizer Kingma (2014) with a learning rate of 0.001, a maximum of 50 epochs, and a dropout rate of 0.1. Quantile loss with $q \in \{0.025, 0.975\}$ was used for 0.95 target coverage.

DeepAR We implemented DeepAR Salinas et al. (2020) using `pytorch_forecasting`. A hyperparameter grid search was conducted on the training set of each dataset with $d_y = 2$ to determine the optimal configuration similarly to TFT. Performance was observed to saturate at a model dimension of 32 with two layers, therefore these settings were used for all experiments. For consistency with FCP, the context window size was fixed at 50 across all experiments. We trained the models using the Adam optimizer Kingma (2014) with a learning rate of 0.001, a maximum of 50 epochs, and a dropout rate of 0.1. Multivariate normal distribution loss with $q \in \{0.025, 0.975\}$ was used for 0.95 target coverage.

Table 3: The hyperparameter search space for FCP.

	Hyperparameter	**Search space**
Vector field	the number of layers	{ 2, 4, 6 }
	hidden dimension	{ 16, 32, 64 }
Encoder	the number of layers	{ 2, 4, 6 }
	the number of heads	{ 2, 4, 8 }
	model dimension	{ 16, 32, 64 }
	dropout	{ 0, 0.1 }
General	covariance scale γ	{ 1, 2, 4, 8 }
	learning rate	{ 0.0005, 0.0001 }
	batch size	{ 8, 16 }

FCP We used multilayer perceptions (MLP) to model the guided vector field $u_{t|h} : [0, 1] \times \mathbb{R}^{d_h} \times \mathbb{R}^{d_y} \to \mathbb{R}^{d_y}$. The time variable $t \in [0, 1]$ was concatenated with the input and fed into the vector field. A hyperparameter grid search was conducted on the training set of each dataset with different d_y to determine the optimal configuration. We set the hidden dimension of the vector field identical to the model dimension of the encoder, so that additional layer is not required between the vector field and the encoder. Table 3 shows the hyperparameter search space and Table 4 shows the optimized hyperparameter configuration. The context window size for the encoder was set to 50. We trained the model with Adam optimizer Kingma (2014) with a maximum of 50 epochs for all experiments and used the validation set to select the best model.

To determine an appropriate sample size N for the set size estimation using quasi-Monte Carlo sampling, we computed the relative standard error of the Jacobian determinants of ψ, defined as

SE($\det J_{\psi,h}$)/Avg($\det J_{\psi,h}$), where $\det J_{\psi,h} = \{\det J_\psi(x_j \mid h)\}_{j=1}^N$ are the sampled Jacobian determinants conditioned on h. We selected the smallest N such that the average relative standard error across all h falls below 0.01. We used $N = 4096$ for experiments with $d_y = 2$, $N = 8192$ for experiments with $d_y = 4$, and $N = 16384$ for experiments with $d_y = 8$.

Table 4: The optimized hyperparameter configuration for FCP based on the grid search.

Dataset	Hyperparameter	$\mathbf{d_y = 2}$	$\mathbf{d_y = 4}$	$\mathbf{d_y = 8}$
Wind	the number of layers of the vector field	4	4	4
	the number of heads of the encoder	2	2	2
	the number of layers of the encoder	4	4	4
	the hidden dimension of the vector field and encoder	32	32	32
	covariance scale γ	1	1	2
	encoder dropout	0.1	0.1	0.1
	batch size	4	4	4
	learning rate	0.0005	0.0005	0.0005
	null condition probability	0.05	0.05	0.05
	guidance scale w (LOO/LSTM base predictor)	1.1/1.1	1.1/1.1	1.1/1.1
Traffic	the number of layers of the vector field	4	4	4
	the number of heads of the encoder	2	2	2
	the number of layers of the encoder	4	4	4
	the hidden dimension of the vector field and encoder	32	32	32
	covariance scale γ	1	1	1
	encoder dropout	0.1	0.1	0.1
	batch size	8	8	8
	learning rate	0.0001	0.0001	0.0001
	null condition probability	0.05	0.05	0.05
	guidance scale w (LOO/LSTM base predictor)	1.1/1.2	1.1/1.2	1.05/1.5
Solar	the number of layers of the vector field	4	4	-
	the number of heads of the encoder	2	2	-
	the number of layers of the encoder	4	4	-
	the hidden dimension of the vector field and encoder	32	32	-
	covariance scale γ	1	1	-
	encoder dropout	0.1	0.1	-
	batch size	8	8	-
	learning rate	0.0005	0.0005	-
	null condition probability	0.05	0.05	-
	guidance scale w (LOO/LSTM base predictor)	1.5/1.2	1.2/1.1	-

B.2 Computational Cost

Training time. Table 5 reports the wall-clock training time for all methods, computed as the sum over five independent runs on five different sequences. All models were trained on a machine equipped with dual Intel Xeon Gold 6226 CPUs and a single NVIDIA A100 GPU. For methods that do not employ neural networks, only the CPU was used.

C Dataset Details

Wind dataset The wind dataset contains wind speed records measured at 30 different wind farms (Zhu et al., 2021). Each wind farm location provides 768 records with 5 features at each timestamp. We randomly select $d_y \in \{2, 4, 8\}$ locations to construct five sequences of d_y-dimensional time series.

Traffic dataset The traffic dataset contains traffic flow collected at 15 different traffic sensor locations (Xu & Xie, 2021b). Each sensor location provides 8778 observations with 5 features at

Table 5: the wall-clock training time (hrs) for all methods.

Dataset	Method	d_y=2	d_y=4	d_y=8
Wind	FCP	≤ 0.2	≤ 0.2	≤ 0.2
	CONTRA	≤ 0.2	≤ 0.2	≤ 0.2
	MultiDimSPCI	≤ 0.05	≤ 0.05	≤ 0.05
	Local Ellipsoid	≤ 0.01	≤ 0.01	≤ 0.01
	Empirical Copula	≤ 0.01	≤ 0.01	≤ 0.01
	Gaussian Copula	≤ 0.01	≤ 0.01	≤ 0.01
	CopulaCPTS	≤ 0.01	≤ 0.01	≤ 0.01
	TFT	≤ 1	≤ 2	≤ 4
	DeepAR	≤ 1	≤ 2	≤ 4
Traffic	FCP	≤ 0.5	≤ 0.5	≤ 0.5
	CONTRA	≤ 0.5	≤ 0.5	≤ 0.5
	MultiDimSPCI	≤ 1	≤ 1	≤ 1
	Local Ellipsoid	≤ 0.01	≤ 0.01	≤ 0.01
	Empirical Copula	≤ 0.01	≤ 0.01	≤ 0.01
	Gaussian Copula	≤ 0.01	≤ 0.01	≤ 0.01
	CopulaCPTS	≤ 0.01	≤ 0.01	≤ 0.01
	TFT	≤ 4	≤ 8	≤ 16
	DeepAR	≤ 4	≤ 8	≤ 16
Solar	FCP	≤ 0.5	≤ 0.5	–
	CONTRA	≤ 0.5	≤ 0.5	–
	MultiDimSPCI	≤ 1	≤ 1	–
	Local Ellipsoid	≤ 0.01	≤ 0.01	–
	Empirical Copula	≤ 0.01	≤ 0.01	–
	Gaussian Copula	≤ 0.01	≤ 0.01	–
	CopulaCPTS	≤ 0.01	≤ 0.01	–
	TFT	≤ 4	≤ 8	–
	DeepAR	≤ 4	≤ 8	–

each timestamp. We randomly select $d_y \in \{2, 4, 8\}$ locations to construct five sequences of d_y-dimensional time series.

Solar dataset The solar dataset considers solar radiation in Diffused Horizontal Irradiance (DHI) units at 9 different solar sensor locations (Zhang et al., 2021). Each location provides 8755 records with 5 features at each timestamp. For the solar dataset, we randomly selected $d_y \in \{2, 4\}$ locations to construct five sequences of d_y-dimensional time series. We did not construct sequences with $d_y = 8$ due to the limited number of unique locations, which could lead to overlapping sequences across different trials of experiments.

D Additional Experiments

D.1 Experiment at 0.9 confidence level

Table 6 reports the results on the three real-world datasets at the 0.9 confidence level. We exclude TFT and DeepAR, as they did not demonstrate competitive performance in the experiment at the 0.95 confidence level. The overall results remain consistent with those at the 0.95 confidence level. Notably, the gap in average prediction set sizes between FCP and other strong baselines—such as MultiDimSPCI, CP using local ellipsoids, and OT-CP for $d_y \in 2, 4$ on the traffic and solar datasets—decreases at the 0.9 confidence level.

D.2 Rolling Coverage on Wind Dataset

Since conditional coverage is challenging to evaluate in real-world data, we use rolling coverage to approximate conditional coverage at a specific time index. Rolling coverage at time index i is

Table 6: Average empirical coverage and prediction sets sizes obtained by FCP and all baselines on three real-world datasets, evaluated under different base predictors and varying outcome dimensions d_y. Reported values represent the average and standard deviation over five independent experiments. The target confidence level was set to 0.9.

Dataset	Base Predictor	Method	$\mathbf{d_y = 2}$		$\mathbf{d_y = 4}$		$\mathbf{d_y = 8}$	
			Coverage	**Size**	**Coverage**	**Size**	**Coverage**	**Size**
Wind	LOO Bootstrap	FCP	$0.906_{\pm.022}$	$0.596_{\pm.050}$	$0.925_{\pm.017}$	$0.734_{\pm.139}$	$0.938_{\pm.011}$	$5.24_{\pm1.45}$
		MultiDimSPCI	$0.917_{\pm.013}$	$0.790_{\pm.341}$	$0.919_{\pm.024}$	$2.26_{\pm1.49}$	$0.933_{\pm.015}$	$47.7_{\pm52.5}$
		CopulaCPTS	$1.000_{\pm.000}$	$22.3_{\pm19.0}$	$1.000_{\pm.000}$	$611.3_{\pm484.7}$	$1.000_{\pm.000}$	$3.50 \times 10^5_{\pm3.73\times10^5}$
		OT-CP	$0.919_{\pm.033}$	$0.904_{\pm.572}$	$0.951_{\pm.025}$	$23.9_{\pm20.9}$	$0.883_{\pm.025}$	$1.00 \times 10^3_{\pm622.8}$
		CONTRA	$0.919_{\pm.045}$	$6.53_{\pm5.17}$	$0.974_{\pm.016}$	$4.12 \times 10^4_{\pm5.05\times10^4}$	$0.974_{\pm.016}$	$4.12 \times 10^9_{\pm4.05\times10^9}$
		Local Ellipsoid	$0.943_{\pm.028}$	$0.952_{\pm.409}$	$0.958_{\pm.015}$	$3.58_{\pm2.18}$	$0.961_{\pm.008}$	$53.2_{\pm68.1}$
		Empirical Copula	$0.914_{\pm.023}$	$0.597_{\pm.204}$	$0.917_{\pm.021}$	$1.21_{\pm.375}$	$0.896_{\pm.042}$	$7.38_{\pm2.04}$
		Gaussian Copula	$0.914_{\pm.023}$	$0.622_{\pm.189}$	$0.917_{\pm.021}$	$1.54_{\pm.725}$	$0.919_{\pm.019}$	$17.0_{\pm4.48}$
	LSTM	FCP	$0.917_{\pm.061}$	$0.884_{\pm.161}$	$0.924_{\pm.024}$	$5.72_{\pm.718}$	$0.896_{\pm.065}$	$848.4_{\pm229.2}$
		MultiDimSPCI	$0.948_{\pm.022}$	$2.68_{\pm1.15}$	$0.904_{\pm.040}$	$41.9_{\pm46.8}$	$0.839_{\pm.074}$	$2.37 \times 10^3_{\pm2.16\times10^3}$
		CopulaCPTS	$1.000_{\pm.000}$	$45.7_{\pm45.4}$	$1.000_{\pm.000}$	$4.82 \times 10^3_{\pm3.73\times10^3}$	$1.000_{\pm.000}$	$2.83 \times 10^7_{\pm3.28\times10^7}$
		OT-CP	$0.909_{\pm.046}$	$5.98_{\pm2.84}$	$0.900_{\pm.029}$	$188.1_{\pm106.3}$	$0.978_{\pm.019}$	$7.21 \times 10^4_{\pm3.49\times10^4}$
		CONTRA	$0.730_{\pm.240}$	$0.22_{\pm.202}$	$0.696_{\pm.247}$	$0.05_{\pm.023}$	$0.761_{\pm.177}$	$7.71_{\pm6.80}$
		Local Ellipsoid	$0.978_{\pm.043}$	$7.40_{\pm4.25}$	$1.000_{\pm.000}$	$167.3_{\pm137.5}$	$1.000_{\pm.000}$	$1.28 \times 10^5_{\pm1.24\times10^5}$
		Empirical Copula	$0.974_{\pm.042}$	$10.6_{\pm5.93}$	$1.000_{\pm.000}$	$325.9_{\pm148.9}$	$0.991_{\pm.017}$	$2.38 \times 10^5_{\pm5.90\times10^4}$
		Gaussian Copula	$0.978_{\pm.043}$	$10.7_{\pm5.86}$	$1.000_{\pm.000}$	$331.4_{\pm131.8}$	$0.991_{\pm.017}$	$3.01 \times 10^5_{\pm1.17\times10^5}$
Traffic	LOO Bootstrap	FCP	$0.913_{\pm.026}$	$0.613_{\pm.243}$	$0.935_{\pm.010}$	$0.453_{\pm.223}$	$0.934_{\pm.039}$	$1.03_{\pm.101}$
		MultiDimSPCI	$0.920_{\pm.008}$	$1.01_{\pm.262}$	$0.929_{\pm.011}$	$1.48_{\pm.468}$	$0.934_{\pm.006}$	$2.92_{\pm.911}$
		CopulaCPTS	$1.000_{\pm.000}$	$21.6_{\pm16.3}$	$1.000_{\pm.000}$	$645.8_{\pm645.5}$	$1.000_{\pm.000}$	$3.18 \times 10^5_{\pm4.80\times10^5}$
		OT-CP	$0.921_{\pm.008}$	$1.09_{\pm.269}$	$0.927_{\pm.010}$	$2.39_{\pm.915}$	$0.914_{\pm.006}$	$1.46 \times 10^3_{\pm588.0}$
		CONTRA	$0.892_{\pm.037}$	$0.606_{\pm.325}$	$0.902_{\pm.034}$	$0.565_{\pm.317}$	$0.849_{\pm.048}$	$0.414_{\pm.309}$
		Local Ellipsoid	$0.927_{\pm.021}$	$1.22_{\pm.391}$	$0.942_{\pm.010}$	$1.17_{\pm.391}$	$0.945_{\pm.008}$	$0.954_{\pm.376}$
		Empirical Copula	$0.915_{\pm.013}$	$1.24_{\pm.296}$	$0.930_{\pm.004}$	$2.17_{\pm.399}$	$0.931_{\pm.004}$	$9.63_{\pm3.17}$
		Gaussian Copula	$0.915_{\pm.012}$	$1.26_{\pm.294}$	$0.934_{\pm.007}$	$2.38_{\pm.501}$	$0.936_{\pm.008}$	$10.9_{\pm1.68}$
	LSTM	FCP	$0.953_{\pm.022}$	$0.633_{\pm.148}$	$0.945_{\pm.019}$	$0.623_{\pm.058}$	$0.923_{\pm.032}$	$0.673_{\pm.298}$
		MultiDimSPCI	$0.914_{\pm.008}$	$0.607_{\pm.255}$	$0.914_{\pm.014}$	$0.977_{\pm.388}$	$0.913_{\pm.022}$	$4.82_{\pm2.70}$
		CopulaCPTS	$1.000_{\pm.000}$	$21.9_{\pm12.7}$	$1.000_{\pm.000}$	$330.0_{\pm219.4}$	$0.999_{\pm.002}$	$4.47 \times 10^5_{\pm4.25\times10^5}$
		OT-CP	$0.894_{\pm.007}$	$0.575_{\pm.238}$	$0.875_{\pm.025}$	$1.99_{\pm1.26}$	$0.850_{\pm.042}$	$356.5_{\pm322.9}$
		CONTRA	$0.889_{\pm.025}$	$0.129_{\pm.050}$	$0.860_{\pm.043}$	$0.031_{\pm.020}$	$0.809_{\pm.060}$	$0.007_{\pm.006}$
		Local Ellipsoid	$0.915_{\pm.028}$	$0.625_{\pm.262}$	$0.899_{\pm.021}$	$0.706_{\pm.325}$	$0.871_{\pm.039}$	$1.12_{\pm.341}$
		Empirical Copula	$0.908_{\pm.015}$	$2.59_{\pm.383}$	$0.912_{\pm.019}$	$13.9_{\pm2.72}$	$0.880_{\pm.020}$	$515.2_{\pm105.7}$
		Gaussian Copula	$0.910_{\pm.017}$	$2.62_{\pm.363}$	$0.908_{\pm.017}$	$13.3_{\pm2.69}$	$0.874_{\pm.019}$	$479.0_{\pm141.1}$
Solar	LOO Bootstrap	FCP	$0.905_{\pm.014}$	$0.589_{\pm.109}$	$0.900_{\pm.010}$	$1.67_{\pm.326}$	-	-
		MultiDimSPCI	$0.930_{\pm.007}$	$1.10_{\pm.068}$	$0.942_{\pm.006}$	$5.13_{\pm.435}$	-	-
		CopulaCPTS	$1.000_{\pm.000}$	$67.9_{\pm12.6}$	$1.000_{\pm.000}$	$7.25 \times 10^3_{\pm1.86\times10^3}$	-	-
		OT-CP	$0.936_{\pm.016}$	$1.44_{\pm.440}$	$0.928_{\pm.009}$	$8.54_{\pm1.84}$	-	-
		CONTRA	$0.889_{\pm.004}$	$1.38_{\pm.506}$	$0.878_{\pm.010}$	$7.16_{\pm4.09}$	-	-
		Local Ellipsoid	$0.897_{\pm.010}$	$0.749_{\pm.064}$	$0.885_{\pm.010}$	$0.320_{\pm.059}$	-	-
		Empirical Copula	$0.949_{\pm.007}$	$1.98_{\pm.192}$	$0.955_{\pm.005}$	$7.87_{\pm.909}$	-	-
		Gaussian Copula	$0.953_{\pm.005}$	$2.12_{\pm.142}$	$0.962_{\pm.004}$	$9.66_{\pm.626}$	-	-
	LSTM	FCP	$0.911_{\pm.051}$	$0.673_{\pm.288}$	$0.907_{\pm.016}$	$0.535_{\pm.104}$	-	-
		MultiDimSPCI	$0.938_{\pm.006}$	$0.733_{\pm.066}$	$0.937_{\pm.004}$	$2.60_{\pm1.04}$	-	-
		CopulaCPTS	$1.000_{\pm.000}$	$44.8_{\pm9.88}$	$1.000_{\pm.000}$	$3.34 \times 10^3_{\pm570.7}$	-	-
		OT-CP	$0.914_{\pm.011}$	$0.585_{\pm.084}$	$0.924_{\pm.019}$	$10.6_{\pm5.80}$	-	-
		CONTRA	$0.835_{\pm.021}$	$0.112_{\pm.037}$	$0.858_{\pm.017}$	$0.034_{\pm.033}$	-	-
		Local Ellipsoid	$0.921_{\pm.012}$	$0.582_{\pm.055}$	$0.934_{\pm.005}$	$0.514_{\pm.250}$	-	-
		Empirical Copula	$0.925_{\pm.005}$	$2.98_{\pm.082}$	$0.939_{\pm.010}$	$17.3_{\pm4.44}$	-	-
		Gaussian Copula	$0.939_{\pm.002}$	$3.56_{\pm.203}$	$0.964_{\pm.005}$	$28.0_{\pm2.64}$	-	-

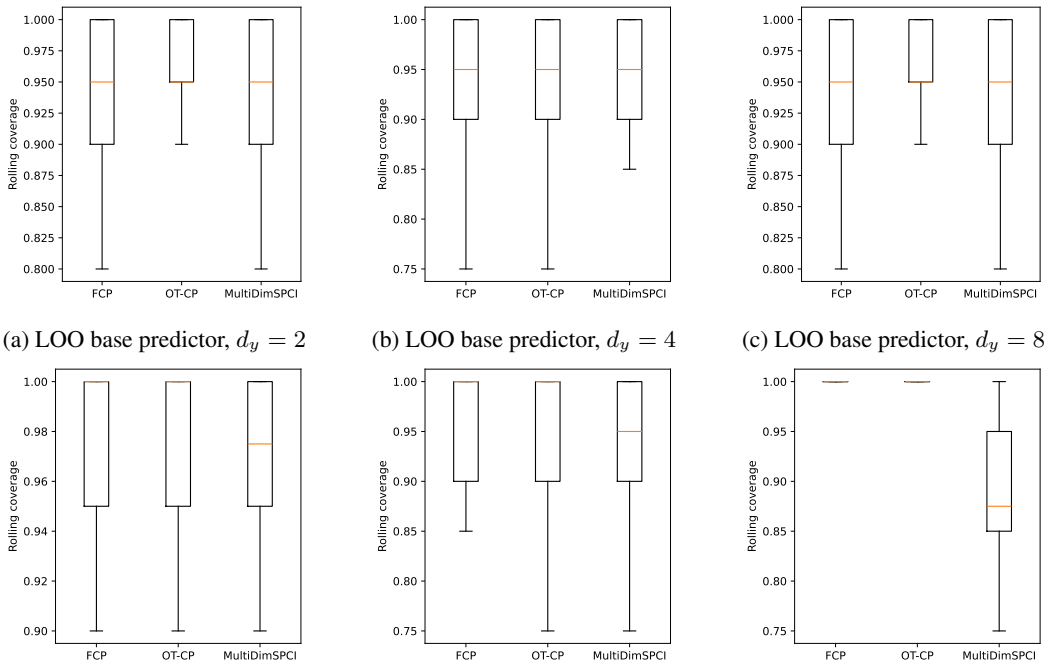

(a) LOO base predictor, $d_y = 2$ (b) LOO base predictor, $d_y = 4$ (c) LOO base predictor, $d_y = 8$

(d) LSTM base predictor, $d_y = 2$ (e) LSTM base predictor, $d_y = 4$ (f) LSTM base predictor, $d_y = 8$

Figure 3: Rolling coverage results on the wind dataset with rolling window size 20.

defined as:

$$\widehat{\mathrm{RC}}_i = \frac{1}{m} \sum_{j=0}^{m-1} \mathbb{1}\left\{ y_{i-j} \in \widehat{C}_{i-j}(z_{i-j}, \alpha) \right\}, \tag{127}$$

where m is a rolling window size. Figure 3 presents the rolling coverage of the test set with rolling window size $m = 20$ on the wind dataset.

D.3 Ablation Study

Ablation study on vector field under bi-Lipschitz flow assumption. Table 7 reports the average empirical coverage and prediction set sizes of FCP with MLP and iResNet across the three datasets with varying d_y.

Table 7: Average empirical coverage and prediction sets sizes obtained by FCP using MLP vector field and iResNet vector field on three real-world datasets, evaluated under different base predictors and varying outcome dimensions d_y. Reported values represent the average and standard deviation over five independent experiments. The target confidence level was set to 0.95. Results with average empirical coverage below the target confidence level are grayed out, and the smallest prediction set sizes, excluding the grayed-out results, are highlighted in bold.

Dataset	Base Predictor	Method	$\mathbf{d_y = 2}$		$\mathbf{d_y = 4}$		$\mathbf{d_y = 8}$	
			Coverage	**Size**	**Coverage**	**Size**	**Coverage**	**Size**
Wind	LOO Bootstrap	FCP (MLP)	$0.951_{\pm.018}$	$\mathbf{0.88}_{\pm.089}$	$0.953_{\pm.006}$	$3.43_{\pm1.37}$	$0.956_{\pm.010}$	$19.4_{\pm10.2}$
		FCP (iResNet)	$0.951_{\pm.021}$	$1.14_{\pm.069}$	$0.954_{\pm.014}$	$\mathbf{1.79}_{\pm.736}$	$0.953_{\pm.018}$	$\mathbf{14.8}_{\pm22.5}$
	LSTM	FCP (MLP)	$0.952_{\pm.054}$	$\mathbf{1.18}_{\pm.215}$	$0.957_{\pm.022}$	$10.8_{\pm1.05}$	$0.953_{\pm.056}$	$\mathbf{2.48 \times 10^3}_{\pm669}$
		FCP (iResNet)	$0.957_{\pm.034}$	$1.84_{\pm.279}$	$0.957_{\pm.018}$	$\mathbf{6.37}_{\pm2.91}$	$0.978_{\pm.015}$	$2.55 \times 10^3_{\pm1.94\times10^3}$
Traffic	LOO Bootstrap	FCP (MLP)	$0.957_{\pm.014}$	$\mathbf{0.915}_{\pm.119}$	$0.953_{\pm.009}$	$\mathbf{1.06}_{\pm.431}$	$0.965_{\pm.015}$	$\mathbf{1.53}_{\pm.161}$
		FCP (iResNet)	$0.950_{\pm.021}$	$1.21_{\pm.084}$	$0.959_{\pm.014}$	$1.33_{\pm.118}$	$0.970_{\pm.007}$	$2.72_{\pm.215}$
	LSTM	FCP (MLP)	$0.968_{\pm.022}$	$0.859_{\pm.075}$	$0.966_{\pm.022}$	$\mathbf{1.05}_{\pm.111}$	$0.950_{\pm.010}$	$\mathbf{1.82}_{\pm.287}$
		FCP (iResNet)	$0.957_{\pm.024}$	$\mathbf{0.788}_{\pm.051}$	$0.970_{\pm.010}$	$1.31_{\pm.103}$	$0.956_{\pm.016}$	$2.50_{\pm.328}$
Solar	LOO Bootstrap	FCP (MLP)	$0.957_{\pm.007}$	$1.48_{\pm.292}$	$0.969_{\pm.003}$	$4.18_{\pm.597}$	-	-
		FCP (iResNet)	$0.952_{\pm.009}$	$\mathbf{1.42}_{\pm.166}$	$0.956_{\pm.003}$	$\mathbf{2.69}_{\pm.196}$	-	-
	LSTM	FCP (MLP)	$0.968_{\pm.009}$	$\mathbf{1.16}_{\pm.092}$	$0.961_{\pm.008}$	$\mathbf{2.09}_{\pm.566}$	-	-
		FCP (iResNet)	$0.955_{\pm.005}$	$1.24_{\pm.076}$	$0.955_{\pm.008}$	$2.42_{\pm.276}$	-	-